ANALYSIS, DESIGN, AND OPTIMIZATION OF SPIRAL INDUCTORS AND TRANSFORMERS FOR SI RF ICS

by

Ali M. Niknejad

ELECTRONICS RESEARCH LABORATORY

Abstract

**Analysis, Design, And Optimization Of Spiral Inductors And
Transformers For Si RF ICs**

by

Ali M. Niknejad

Master of Philosophy in Engineering-Electrical Engineering and Computer Sciences

University of California

Professor Robert G. Meyer, Chair

Si IC spiral inductors and transformers are analyzed using electromagnetic analysis. With appropriate approximations, the calculations are reduced to electrostatic and magnetostatic calculations. The important effects of substrate loss are included in the analysis. Classic circuit analysis and network analysis techniques are used to derive two-port parameters from the circuits. From two-port measurements, low-order frequency-independent lumped circuits are used to model the physical behavior over a broad-frequency range. The analysis is applied to traditional square and polygon inductors and transformer structures, as well as to multi-layer metal structures. A custom CAD tool *ASITIC* is described, used for the analysis, design, and optimization of these structures. Measurements taken over a frequency range from 100 MHz to 5 GHz show good agreement with theory.

Table of Contents

Acknowledgments

First and foremost I would like to thank my advisor, Prof. Robert G. Meyer, for giving me the opportunity to work on such an exciting problem. His help, support, and guidance has been outstanding. I would also like to thank Ranjit Gharpurey for his support and guidance. He has acted as a friend and as a co-advisor and I have learned a lot by working with him. Also, I would like to thank Prof. Paul R. Gray for his support and guidance, especially during the 1995-96 during which time he acted as a advisor in Prof. Meyer's absence. Finally I would like to thank Prof. Bernhard Boser for acting as the second reader the thesis.

I also thank Bill Mack for his help and support in fabricating the test structures. The help of Janice Eisenstadt and Yen Nguyen of Philips Semiconductors in measuring the test structures is also greatly appreciated.

I must also thank the companies and individuals who have given me the opportunity to work on this problem during the summer. I thank T.R. Viswanathan and Texas Instruments for their support. I also thank Mihai Banu and Lucent Technologies for their support.

I must thank all of my colleagues that I have interacted with in the past few years. They have made my experience rich and satisfying. I thank Manolis Terrovitis, Keng Leong Fong, John T. Wetherell, Darrin Young, Sang Won Son, Kevin J. Wang, Joel King, Tom Naiyavudhi, Li Lin, George Chien, Jeff Jia-Jiunn Ou, Matrin Tsai, Sekhar Narayanaswami, and Chris Rudell.

Last, but certainly not least, I am gratefully indebted to my close family and friends. I thank my parents for their friendship and support, and especially my father for introducing me to the exciting world of electronics. I thank my sisters for their friendship and their guidance. I thank my friend Alexandra for her love and friendship.

Chapter 1: Introduction

Si ICs are finding wide application in the GHz frequency range. Modern bipolar, CMOS, and BiCMOS processes provide high f_T transistors allowing Si RF-ICs to compete with GaAs ICs in the important low GHz frequency ranges. However, the lossy Si substrate makes the design of high Q reactive components difficult. Despite this difficulty, the low cost of Si IC fabrication over GaAs IC fabrication and the potential for integration with baseband circuits makes Si the process of choice in many RF IC applications.

The demands placed on portable wireless communication equipment include low cost, low supply voltage, low power dissipation, low noise, high frequency of operation and low distortion. These design requirements cannot be met satisfactorily in many cases without the use of RF inductors. Hence, there is a great incentive to design, optimize, and model spiral inductors fabricated on Si substrates. This topic is addressed in this paper.

Since the introduction of Si spiral inductors [1], many authors have reported higher performance inductors on Si substrates, primarily utilizing advances in processing technology. This has included higher conductivity metal layers to reduce the loss resistance of the inductor [2], use of multi-metal layers to increase the effective thickness of the spiral inductor and thereby reduce loss, the connection of multi-metal layer spirals in series to reduce the area of the inductors [3][4], low-loss substrates to reduce losses in the substrate at high frequency [5], and thick oxide or floating inductors to isolate the inductor from the lossy substrate [6]. Little, though, has been written on the analysis and optimization of these structures.

In [7] an analysis approach is presented where an equivalent circuit for each segment of the spiral is calculated and the inductor is considered as an interconnection of such segments. The approach is limited, though, as many important effects are not included. For instance, non-uniform current distribution due to skin and proximity effects

within each segment is not considered. In addition, the impedance to substrate is calculated using a 2-dimensional approach, making it difficult to apply to arbitrary structures or to coupled inductors.

Most past researchers have used measurement results on previously built inductors to construct models. While this technique is most practical, it does not allow the possibility of optimization nor does it allow the circuit designer freedom to choose parameters such as inductance, resistance, capacitance and Q. Otherwise researchers have used commercial 3D electromagnetic simulators [8][9] to design and analyze inductors and transformers. While this approach is accurate, it can be computationally very expensive and time-consuming. This prevents the designer from performing optimization. In this paper we present an accurate and computationally efficient approach to overcome some of these difficulties.

Chapter 2: The Electric and Magnetic Integral Equations

In this chapter, the basic problem is formulated and the analysis technique is outlined. In section 2.1 we examine the important physical phenomena that give rise to inductance and other parasitic effects for passive inductors and transformers over the Si substrate. Our discussion will be at first qualitative in order to gain physical insight into the problem. Next, in section 2.2, we examine the problem more rigorously. By making appropriate assumptions, the problem will be simplified by reduction to electrostatic and magnetostatic equations.

2.1 Qualitative Discussion of the Physics of Inductors and Transformers

A typical spiral inductor has geometry as shown in Fig. 1. Qualitatively, the spiral inductor consists of a number of series-connected metal segments. In each segment, time-varying conductive current will flow due to a time-varying voltage impressed on the segment. In addition, due to self-inductive and mutual-inductive effects (i.e. magnetic flux
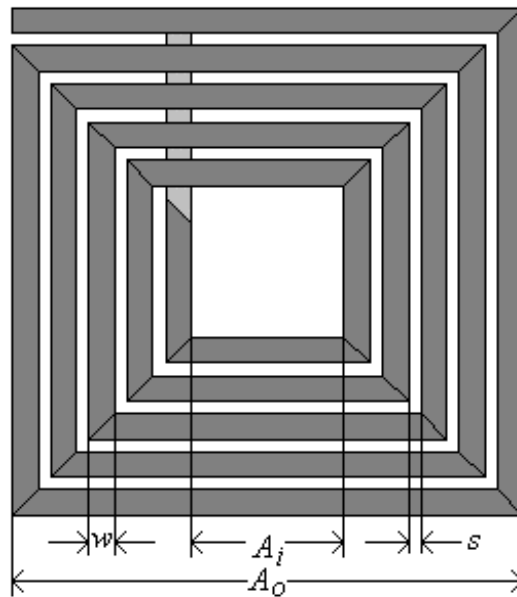

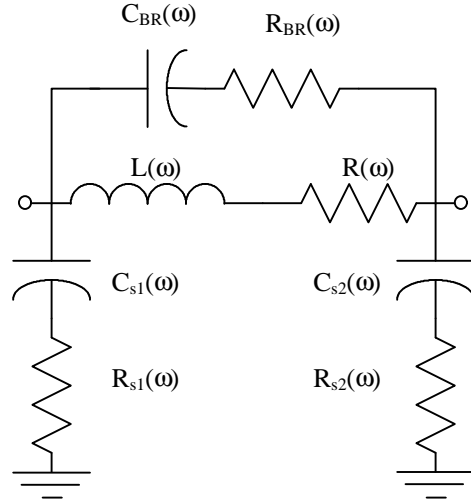Fig. 1. Layout of a typical square spiral inductor.

Fig. 2. Frequency-dependent model of spiral.

linkage from segment to segment) a time varying emf is produced with a phase 90° leading the impressed conductive current. Furthermore, due to the presence of the substrate and closely spaced metal segments, charge on each segment will cause charge to accumulate and flow at the surface of the substrate as well on neighboring segments. This charge will flow as a current 90° lagging the impressed voltage. Due to the finite conductivity of the substrate, the induced substrate charge must flow through the lossy substrate, acting as an additional source of loss.

The equivalent circuit of Fig. 2 can be used as a model for the spiral. In the figure, $L(\omega)$ models the frequency dependent inductive effects of the spiral by combining all sources of reactance that cause current to lag by 90°. It shows frequency dependence since the magnetic field and current distributions in the segments will change due to current constriction (skin-effect) and proximity effects of neighboring segments. $R(\omega)$ models the loss due to the finite conductivity of the metal segments and its frequency effects are also due to current constriction and proximity effects. In addition, at very high frequency, time retardation effects become important and R can also model the radiation resistance. To model interwinding impedance we use $C_{BR}(\omega)$ and $R_{BR}(\omega)$. The interwinding capacitance is lossy since segments are not only linked through the oxide but also through the substrate. Its frequency dependence is due to the substrate impedance.

At lower frequency, when the substrate acts like a good ground plane, the substrate will partially shield segments from each other. But at higher frequency, due to the finite time constant of the substrate, as well as the non-zero impedance that grounds the substrate externally, the substrate will begin to float electrically. In this situation, the substrate will not shield metal segments as effectively, and the effective coupling capacitance will increase.

Finally, $C_s(\omega)$ and $R_s(\omega)$ model the substrate current injection and reception. $C_s(\omega)$ represents the capacitance from the metal segments to the substrate; $R_s(\omega)$ models the substrate loss. Both are frequency dependent due to the frequency dependence of the substrate conduction. At high frequency, current in the substrate can flow due to displacement as well as conductive mechanisms. In addition, the external grounding circuits, typically bond-wires, have finite impedance. Note that the equivalent circuit is almost symmetric. The outer segments of the spiral are longer and have more volume to support fringing fields whereas inner turns are shorter and less capacitive. The outermost turn has additional volume for fringing fields outside of the area of the spiral itself. This would tend to make the outer port of the spiral more capacitive. The inner turn, however, has an additional bridging segment of higher capacitance located on the lower metal layers.

In addition to the above effects, many other higher-order effects are present. For instance, eddy-currents flow in the substrate due to the penetration of time varying magnetic fields in the substrate. Additionally, currents induced in the substrate give rise to secondary magnetic fields which interact with the primary magnetic fields impressed by the current of the metal segments. These effects can be modeled by adding additional frequency dependent loss to $R(w)$. The secondary magnetic fields generated by substrate currents can be modeled by adding a secondary port to the model of Fig. 2, coupled with coefficient $k(w)$, which of course is also frequency dependent.

2.2 Electromagnetic Formulation

Consider a typical spiral inductor or transformer. It consists of series and parallel interconnection of metal segments. Applying Maxwell's equations to the conductive portions of such a structure, we obtain [10]

$$\int E_0 \cdot dl - \int \frac{J}{s} \cdot dl - \int \frac{\partial A}{\partial t} \cdot dl - \int \nabla f \cdot dl = 0 \tag{1}$$

where E_0 is the applied field, J is the current density, s is the conductivity of the metal segment, A is the magnetic vector potential, and f is the electric scalar potential. The first term of the above equation arises from the applied field, the second term represents the internal impedance of the segments, the third term represents external inductance, and the fourth term is the capacitive term.

To see how the third term represents the external inductance, apply Stoke's theorem to get

$$\oint \frac{\partial A}{\partial t} \cdot dl = \frac{d}{dt} \oint A \cdot dl = \frac{d}{dt} \int_S (\nabla \times A) \cdot dS = \frac{d}{dt} \int_S B \cdot dS \tag{2}$$

from circuit theory therefore

$$\oint \frac{\partial A}{\partial t} \cdot dl = L \frac{dI}{dt} \tag{3}$$

The magnetic and electric potentials are integrals over the charges and currents in the circuit. In the time-periodic case we have

$$f(x, y, z) = \int_V \frac{r(x', y', z')e^{-jkR}}{4 p e R} dV' \tag{4}$$

$$A(x, y, z) = m \int_V \frac{J(x', y', z')e^{-jkR}}{4 p R} dV' \tag{5}$$

The above retarded potentials can be simplified to static potentials since at frequencies of interest the exponential term is nearly unity. As they stand, though, the above equations are impractical since they involve integrating over all charges and currents, including those that flow through the substrate. If, however, we replace the R^{-1} term involving the free-space Green function with the appropriate Green functions over a multi-layer substrate,

the volume of integration reduces to metal segments containing the charges and currents. In chapter 5 we derive the electrostatic Green function over a multi-layer conductive substrate which can be used in (4). Hence (4) and (5) can be written

$$f(r,t) = \sum_k \frac{1}{4pe} \int_{V_k} G_E(r,r') r(r') dV' \tag{6}$$

$$A(r,t) = \sum_k \frac{m}{4p} \int_{V_k} G_M(r,r') J(r') dV' \tag{7}$$

where the index k runs through the conductors which make up the device. The above quasi-static approximations simplify the problem greatly. From Maxwell's equations and the definition of the magnetic vector potential we have

$$\begin{aligned} \nabla \times E &= -jwB \\ B &= \nabla \times A \end{aligned} \tag{8}$$

Combining the above equations we have

$$\nabla \times (E + jwA) = 0 \tag{9}$$

Since the curl of the above relation is identically zero, one can find a scalar potential whose gradient is equal to parenthetical expression of (9)

$$E + jwA = -\nabla f \tag{10}$$

Using equations (10) and (7), and assuming a linear constitutive relation between J and E, we have for each segment

$$\frac{J_i(r)}{s_i} + \frac{jwm}{4p} \sum_k \int_{V_k} J_k(r) G_M(r,r') dV' = -\nabla f_i \tag{11}$$

In general, the current density is non-uniform across the cross-section of each segment. The non-uniformity is due to current constriction and proximity effects. These effects make (11) difficult to solve directly. If, however, we discretize the cross-section into b sections of constant current density [11][12], then (11) will take on a more tractable form. In other words assume J_i can be approximated by

$$J_i(r) = \sum_{m=1}^{b} I_{i,m} w_{i,m}(r) \vec{l}_m \tag{12}$$

where $I_{i,m}$ is current inside the sub-segment m of segment i, $\vec{l}_m$ is a vector in the direction of the segment, and $w_{i,m}$ is a function that has a value of $1/a_{i,m}$ inside the cross-section and

zero outside, where $a_{i,m}$ is the cross-sectional area of sub-segment m of segment i. Using equation (12), it can be shown that equation (11) becomes [12]

$$\left(\frac{l_i}{\boldsymbol{s}a_{i,m}}\right)I_{i,m} + j\boldsymbol{w}\sum_k \sum_{j\in S_k}\left(\frac{\boldsymbol{m}}{4\boldsymbol{p}a_{i,m}a_{j,m}}\iint_{v_i v_j}\vec{l}_i\cdot\vec{l}_j G_M(r,r')dV'dV\right)I_{j,m} = \frac{1}{a_{i,m}}\int_{a_i}\Delta\boldsymbol{f}_{i,m}dA \quad (13)$$

where S_k is the set of indices of the sub-segments of segment k. The above equations can be simplified if we make the assumption that the potential drops across parallel sub-segments are equal, or $\Delta\boldsymbol{f}_{i,m} = \Delta\boldsymbol{f}_i$. In chapter 5 we will show that this assumption simplifies the above equation to

$$Z_{ii}^L I_i + j\boldsymbol{w}\sum_k Z_{ik}^L I_k = \Delta\boldsymbol{f}_i \quad (14)$$

or in matrix notation

$$[\Delta\boldsymbol{f}] = [Z^L][I] \quad (15)$$

where the matrix $[Z^L]$ has diagonal entries representing the internal impedance of each segment and the off-diagonal terms represent the external magnetic coupling from segment to segment. Equation (15) alone, though, is not enough since both the potentials and the currents in the segments are unknowns. But the potential at each segment is also related to the charge distribution by (6). We seek to find the potential of segment i, due to a charge distribution on segment j. If we partition the segments into sufficiently small segments i and j, we may assume uniform charge distribution and take the potential of the segment to be the average potential over the volume. For these approximations, we obtain

$$\bar{\boldsymbol{f}}_i = \frac{Q_j}{V_j V_i}\iint_{V_i,V_j}G_E dV_j dV_i \quad (16)$$

By considering the above integral for all combinations of segments, we generate the following matrix equation

$$[\boldsymbol{f}] = [P][Q] \quad (17)$$

The matrix $[P]$ is known as the coefficient-of-potential matrix. By inverting the above relation we form the coefficient-of-induction matrix and henceforth we have the desired charge distribution

$$[Q] = [c][\boldsymbol{f}] \quad (18)$$

Alternatively, we may rewrite (18) in terms of the potential differences as

$$[Q] = [C][\Delta f] \tag{19}$$

where $[C]$ is the familiar capacitance matrix. Charge conservation at each segment implies that

$$\Delta I_i = \dot{Q}_i = jwQ_i \tag{20}$$

where ΔI_i is net current flowing into segment i which must equal the rate of change of charge depositing on the segment. Thus

$$\Delta I_i = jwQ_i = jw e_i^T [C][V] \equiv e_i^T [Z^C][V] \tag{21}$$

where e_i is the unit vector with one in entry i and zero everywhere else, and $[Z^C]$ is the capacitive impedance matrix. We can account for the finite conductivity of the substrate in the capacitive impedance matrix calculation as follows. From Maxwell's equation we have

$$\nabla \times B = jwD + J = jwD + sE = jw(e + \frac{s}{jw})D = jw e_{eff} D \tag{22}$$

where we have defined an effective frequency-dependent complex permittivity. If we use this effective permittivity in deriving our Green function, then the losses due to the finite conductivity of the substrate will be accounted for by the real part of the Z^C matrix.

Equations (14) and (21) form a complete system of equations which can be solved at each frequency to obtain the voltages and currents in the segments.

Chapter 3: Circuit Analysis

In the next two chapters we will show how to extract circuit parameters from the geometric layout of an inductor or transformer. In this chapter we will consider the interconnection of these various conductors and the resulting current-voltage characteristics of interest in the design of circuits.

3.1 Circuit Equation Formulation

From a circuit point of view, equations (2.14) and (2.21) can be interpreted as shown in Fig 1. To derive the 2-port parameters of such a structure, we must solve the circuit equations by selecting an appropriate number of independent equations, using for instance nodal or loop analysis. Let us consider the topology of the network in relation to the spiral. For a typical p-sided spiral of n turns, there are $s=n{\times}p$ segments. Each segment has one branch associated with the series inductance and resistance, and one branch associated with the substrate impedance. Assuming a dense capacitive coupling impedance matrix, then this adds an additional $s(s-1)/2$ branches of lossy capacitors from segment to segment. Hence, the total number of branches $B = (s+1)(s+2)/2$. The total number of nodes N in the circuit is simply one plus the number of segments, or $s+1$.
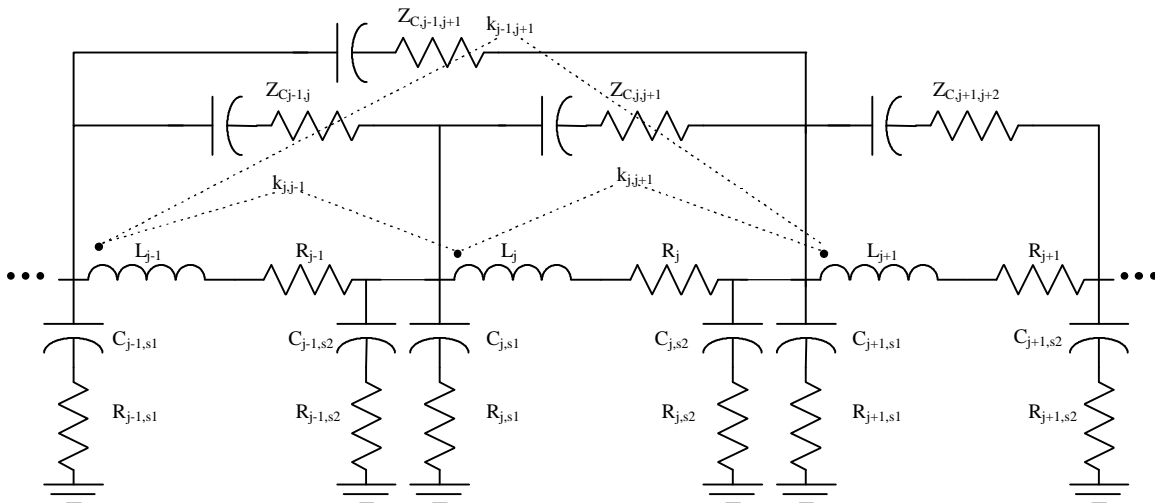

Fig. 1. Equivalent circuit model of spiral segments.

Consequently, the total number of fundamental loops L in the circuit equals $L=B-N\sim O(s^2)$.

Although loop equations are a more natural formulation, due to the mutual inductive nature of the circuit, the number of required equations is one order of magnitude larger than the number of node equations. Hence, nodal analysis is the method of choice. Writing the nodal equations at node j results

$$\frac{V_j}{Z_{j0}^C} + \sum_{k\neq j}\frac{V_j}{Z_{jk}^C} - \sum_{k\neq j}\frac{V_k}{Z_{jk}^C} + I_j - I_{j-1} = 0 \tag{1}$$

In the above equation, V_j is the voltage at node j, I_j is the current flowing into segment j, Z_{jk}^C is the lossy capacitive impedance coupling segment j and k. The above equations involve the voltages and currents in the segments, similar to modified nodal analysis. The voltage across each segment is related to the currents flowing in the segments by

$$V_j - V_{j+1} = \sum_k Z_{jk}^L I_k \tag{2}$$

where Z_{jk}^L is an entry of the symmetric inductance matrix Z^L. The diagonal terms represent the internal impedance of each segment whereas the off-diagonal terms represent the magnetic coupling between segments. The above system of equations yields an invertible complex frequency-dependent matrix. Since there are $2s$ equations in (1) and (2), the system can be solved directly using Gaussian elimination with pivoting or LU factorization, in time $O((2s)^3)$. However, the matrix naturally partitions into four square matrices as

$$\begin{bmatrix} Y^C & D^T \\ D & -Z^L \end{bmatrix}\begin{bmatrix} V \\ I \end{bmatrix} = \begin{bmatrix} I_s \\ V_s \end{bmatrix} \tag{3}$$

Y^C is a matrix with elements

$$[Y_{ij}^C] = \frac{-1}{Z_{ij}^C} \qquad\qquad [Y_{ii}^C] = \sum_k \frac{1}{Z_{ik}^C} \tag{4}$$

D is an upper-triangular band matrix with its diagonal entries as 1 and with super diagonal entries as -1. Rewriting (3) we have

$$(Y^C + D^T Y^L D)V = I_s + D^T Y^L V_s \tag{5}$$

$$I = Y^L (DV - V_s) \tag{6}$$

15

where $Y^L = (Z^L)^{-1}$ is the inverse of the inductance matrix. As we will see later, Y^L is known a priori and no explicit matrix inversion needs to be performed. In addition, due to the simple structure of D, the matrix products involving D and its transpose can be done in $O(s^2)$. Hence, in forming (5) and (6) no explicit matrix products need to be formed. Thus, we can solve (5) by using an *LU* decomposition of $(Y^C + D^T Y^L D)$ and then solve (6) directly for *I*. Therefore, the solution of (3) is dominated by one *LU* decomposition of an $s \times s$ matrix, which can be performed in time $O(s^3)$. This is more than eight times faster than solving (3) directly.

3.2 Low-Frequency Network Analysis

In the previous section the complete matrix inverse was found for a dense capacitive and inductive matrix. In practice, it is not uncommon for the capacitive matrix to be sparse, especially if the approximations are employed. In this case, sufficiently far from self-resonant frequency, one can obtain the two port parameters for the entire spiral in $O(n)$ time.

The approximation is to treat each segment of the spiral as an effective two-port. Clearly, each segment is not a two-port since it interacts with all other segments both capacitively and inductively. Far from self-resonance, though, the segments act inductively and negligible current will flow through coupling capacitors and into the substrate. Using this approximation, equation (4.19) becomes

$$V_i \approx \left(\sum_{k \in C_i} Z_{ik}^L + \sum_{k \notin C_i} jwL_{ik} \right) I = Z_{i,eff}^L I \tag{7}$$

where *I* is the total AC current driving the spiral. This approximation yields an effective series impedance. In addition, if we neglect all mutual capacitive coupling except for segments which neighbor one another, or in other words if we only consider turn to turn interwinding capacitance, then each turn of the *p*-spiral can be considered as a cascade of *p* effective segment two ports. Fig. 2 illustrates this idea. Each segment is represented by

a pi-circuit similar to Fig. 1 but the lumped impedance and admittance of segment i are given by

$$L_i = \text{Im}[Z_{i,\text{eff}}^L] \qquad\qquad R_i = \text{Re}[Z_{i,\text{eff}}^L] \tag{8a}$$

$$C_{s,i} = \tfrac{1}{2}\text{Im}[Y_{i0}^C] \qquad\qquad R_{s,i} = 2\,\text{Re}[Y_{i0}^C] \tag{8b}$$

lumping the mutual inductive effects in L_i and R_i. The ABCD parameters of the segment are given by [13]

$$A = 1 + \frac{y_2}{y_3} \tag{9a}$$

$$B = \frac{1}{y_3} \tag{9b}$$

$$C = y_1 + y_2 + \frac{y_1 y_2}{y_3} \tag{9c}$$

$$D = 1 + \frac{y_1}{y_3} \tag{9d}$$

where
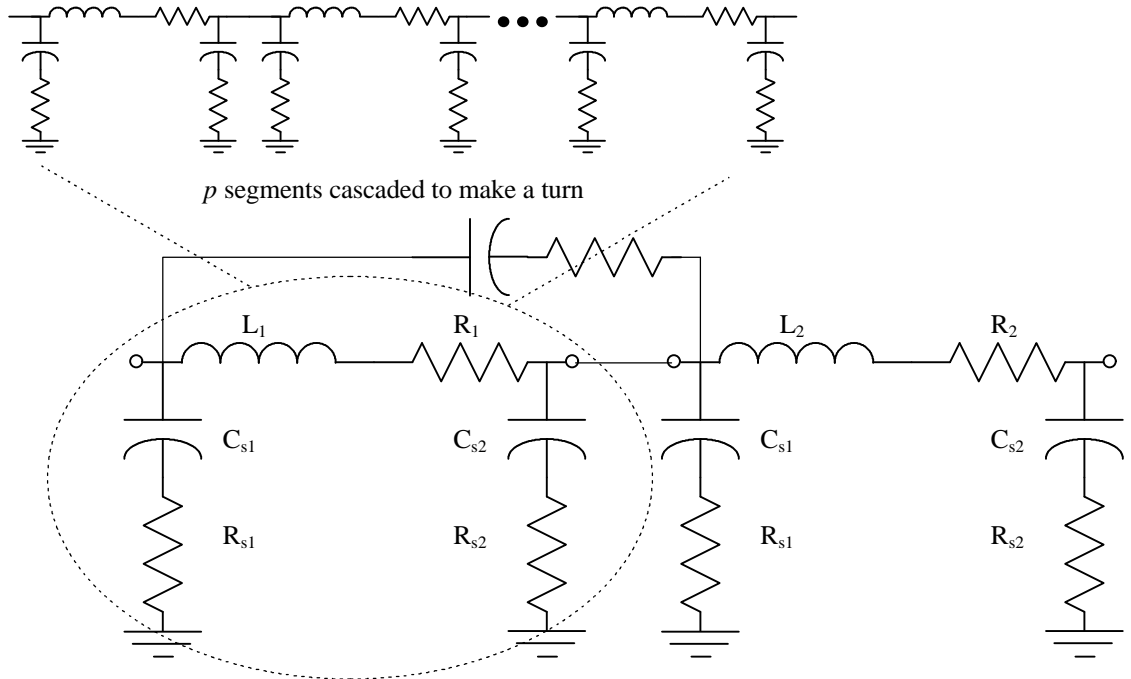
Fig. 2. Equivalent two-port representation of a single turn of a spiral.

$$y_1 = y_2 = \cfrac{1}{\cfrac{1}{jwC_{s,i}} + R_{s,i}} \qquad y_3 = \frac{1}{jwL_i + R_i} \qquad (10)$$

Utilizing the above equations, the cascade of p two-ports can be performed to find the equivalent two-port for one entire turn. The resulting two-port ABCD parameters are converted to y-parameters, since the effective turn-to-turn capacitance appears in shunt with the turn two-port matrix. After performing a similar calculation for each turn of the spiral, the overall y-matrix parameters can be derived by cascading all the turns of the spiral.

The above approximation works well far from the self-resonant frequency where the approximation made in equation (7) holds. This approximation may be refined near resonance in an iterative fashion as follows. First, we perform the above described computation, and as matrix multiplication is performed, we save the results of the node voltages V_i. Then we begin an iteration where we repeat the above calculation with the following modifications. First, in computing the effective series impedance of each segment, we utilize (4.19) directly where I_n is given by

$$I_n = I - \sum_{i=1}^{n-1} \frac{V_i}{Z_{i0}^C} - \sum_{i=1}^{n-1} \sum_{j=n+1}^{N} \frac{V_i - V_j}{Z_{ij}^C} \qquad (11)$$

The above equation is exact and is derived by KCL, where I is the total current injected into the spiral, and the first term subtracted represents current lost to the substrate and the second term represents current flowing through the interwinding impedance. Although the V_i are unknown, they may be approximated by the previous iteration. The above iteration is performed until sufficient accuracy is obtained. This provides the two-port parameters of the spiral in $O(n)$ time.

Chapter 4: Inductance Matrix Calculation

In Chapter 2 we de-coupled the electric and magnetic field calculations. This simplified the inductance matrix calculation tremendously. In this chapter we will outline some practical techniques to calculate the inductance of metal segments which constitute our inductors and transformers. Although we will use the term inductance freely in the following discussion, we often mean partial inductance rather than inductance. The important difference between these two terms is explained [14]. The distinction, though, should be clear in context.

First, we will tackle the calculation of inductance at zero frequency, when the current distribution across the width of our conductor segments is uniform. This leads naturally to the Geometric Mean Distance (GMD) approximation which is used widely. Next, we consider the problem at high frequency, when the current in the conductors becomes non-uniform. We already alluded to this earlier in our discussion in Chapter 2 where we proposed to approximate the conductor by finitely many constant current sections. This leads naturally to the concept of calculating the inductance matrix, with diagonal entries corresponding to the impedance of each metal segment and off-diagonal terms corresponding to mutual inductive coupling. The matrix is naturally symmetric, due to the reciprocal nature of the physics.

4.1 Geometric Mean Distance Approximation

If we apply the free space Green function to equation (2.13) we obtain an expression for the mutual inductance between segments

$$M_{ij} = \frac{\mu}{4\pi a_i a_j} \iint_{V_i V_j} \frac{\vec{l}_i \cdot \vec{l}_j}{|r - r'|} dV' dV \tag{1}$$

which may be evaluated to yield the mutual inductance matrix. By employing the GMD approximation, we can compute the self and mutual inductance of an arbitrary arrangement of conductors in closed form. Fig. 1a shows two infinitesimally thin current
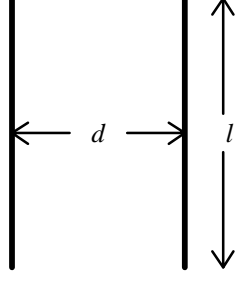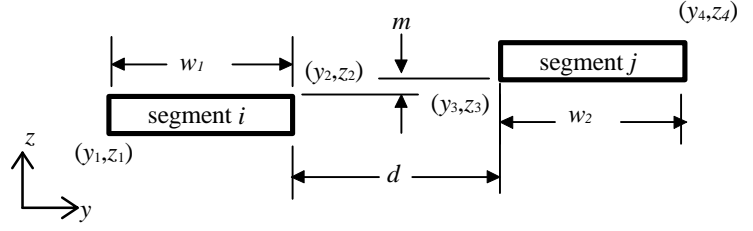
Fig. 1a. Layout of current filaments.   Fig. 1b. Cross-section of rectangular metal segments.

filaments of length l separated by a length d. The mutual inductance between these filaments may be evaluated in closed form using equation (1). The result is given by [15]

$$\text{M}(l,d) = 2 \times 10^{-4} \times l \times \left[\ln\left(\sqrt{1+\left(\frac{l}{d}\right)^2} + \frac{l}{d} \right) - \sqrt{1+\left(\frac{d}{l}\right)^2} + \frac{d}{l} \right] \qquad (2)$$

where lengths are given in μm and M is in nH. For a typical geometry of interest, $l \gg d$, hence we neglect the term $\left(\dfrac{d}{l}\right)^2$. This leads to

$$M = 2 \times 10^{-4} \times l \times (\frac{d}{l} - \ln(d) + \ln(2l) - 1) \qquad (3)$$

In order to find the mutual inductance between two equal length conductors separated by a fixed distance with arbitrary cross-sectional areas, we compute the following integral utilizing equation (2)

$$M_{A,B} = \iint\limits_{A_A A_B} \text{M}(l,d)\, dA_A\, dA_B \qquad (4)$$

If equation (3) is used as an approximation, then d is the only variable under integration. Integrating equation (3), the first term leads to the mean distance between the two cross-sectional areas, or the Arithmetic Mean Distance (AMD). The second term leads to the Geometric Mean Distance, or GMD, the mean of $\ln(d)$ as d takes on the distance between all points within the two cross-sectional areas.

For self-inductance, we average equation (3) over the area of a single conductor. This leads to the GMD and AMD of an area from itself. For a rectangular cross-section of

width w and thickness t, this integral may be computed exactly, but the following approximation offered by [15] serves well

$$L = 2 \times 10^{-4} \times l \times \left[\ln\left(\frac{2l}{w+t}\right) + 0.5 \right] \tag{5}$$

To compute the mutual inductance between two rectangular conductors shown in Fig. 1b, we must calculate the GMD and AMD. The GMD is found by integrating

$$\iint_{A_1} \iint_{A_2} \log \sqrt{(y-y')^2 + (z-z')^2}\, dy'\, dz'\, dy\, dz \tag{6}$$

The above integral can be evaluated exactly [11] by observing that

$$\frac{\partial^4 \, \mathrm{F}(y-y', z-z')}{\partial y\, \partial z\, \partial y'\, \partial z'} = -\ln[(y-y')^2 + (z-z')^2] - \frac{25}{6} \tag{7}$$

where

$$\mathrm{F}(y,z) = \frac{(y^4 - 6y^2 z^2 + z^4)}{24} \ln(y^2 + z^2) - \frac{yz}{3}(y^2 \tan^{-1}\frac{z}{y} + z^2 \tan^{-1}\frac{y}{z}) \tag{8}$$

Using the above observation for the geometry in Fig. 1b, equation (6) evaluates to

$$-\frac{1}{2}\mathrm{F}(y-y', z-z')\Big|_{y_1}^{y_2}\Big|_{y_3}^{y_4}\Big|_{z_1}^{z_2}\Big|_{z_3}^{z_4} - \frac{25}{12} w_1 w_2 t_1 t_2 \tag{9}$$

For the case of infinitely thin conductors, the above simplifies to

$$-\frac{3}{2}w_1 w_2 + \sum_{k=b,g;\, j=a,d} m(k \tan^{-1}\frac{k}{m} - j \tan^{-1}\frac{j}{m}) + \sum_{k=b,g;\, j=a,d} \frac{m^2}{2}(\log(1+\frac{j^2}{m^2}) - \log(1+\frac{k^2}{m^2})) +$$

$$\sum_{k=b,g;\, j=a,d} \frac{1}{2}((m^2 + k^2)\log\sqrt{1+\frac{j^2}{m^2}} - (m^2 + j^2)\log\sqrt{1+\frac{k^2}{m^2}})$$

where

$$a \equiv d + w_2, \, b \equiv d$$
$$g \equiv d + w_1, \, d \equiv d + w_1 + w_2 \tag{10}$$

where d is the horizontal distance between the conductor inner edges and m is the vertical distance between the conductors. Although equations (9) and (10) are complex, they can be handled effectively by computer analysis. Further simplifications to the geometry of (10) lead to simple equations. For instance, for equal width conductors of negligible
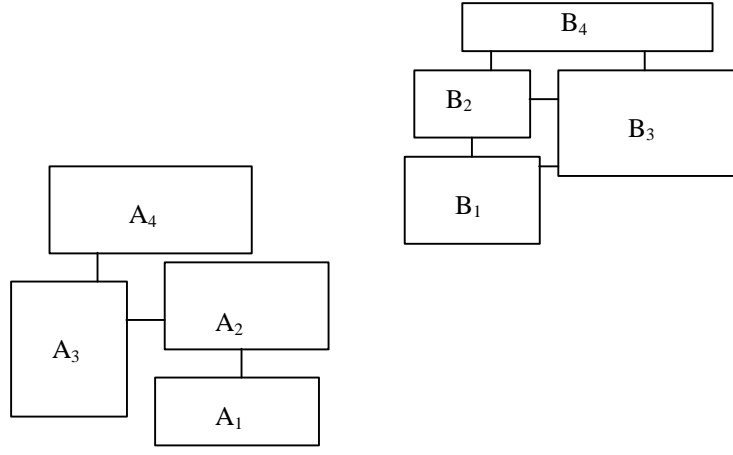
Fig. 2. Cross-section of multi-rectangular metal segments.

thickness, (10) takes on a simple form. The GMD for these simple cases can be found in [15]. Alternatively, simplifications such as power series expansions or polynomial approximation may be used.

We have found the GMD of two equal length parallel conductor segments. These results may be used to build more complex cross-sections by using the rules of GMD found in [15]. Consider the N conductor cross-sections shown in Fig. 2, each cross-section i has an area A_i and a GMD to itself R_{ii}, and a GMD to other cross-sections R_{ij}. If we assume that the N cross-sections form a new cross-section, then we would like to find the total effective GMD of this cross-section to itself. The new GMD of the total conductor from itself R_s is given by

$$\log R_s = \frac{\sum_{i=1}^{N} \sum_{j=1}^{N} A_i A_j \log R_{ij}}{(\sum_{i=1}^{N} A_i)^2} \tag{11}$$

In the above equation, the R_{ij} may be calculated by equation (9). Furthermore, for the above system of N cross-sections, we can find the effective GMD to a system of M other cross-sections of area B_i shown in Fig. 2 by the following

$$\log R_{M,N} = \frac{\sum_{p=1}^{N} A_p \log\left(\sum_{k=1}^{M} B_k \log R_{B_k A_p}\right)}{\sum_{p=1}^{N} A_p \sum_{k=1}^{M} B_k} \tag{12}$$
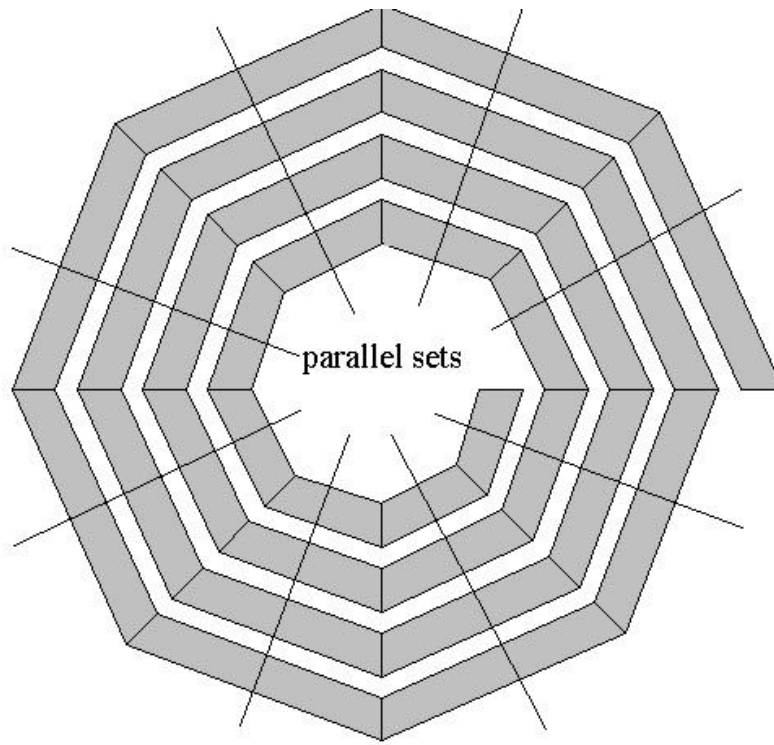
22

Fig. 3. Layout of polygon spiral.

where $R_{B_k A_p}$ is the GMD from B_k to A_p. The above equations can be used to calculate the GMD of more complex cross-section. Using the GMD, self and mutual-inductance can be calculated using (2).

The above discussion has concentrated on equal-length parallel conductors. This is an important special case as it occurs frequently in the analysis of spirals. As shown in Fig. 3, the layout of a typical non-rectangular spiral contains many segments which are not parallel. But the set of segments which couple most strongly tend to be parallel; such a typical set is highlighted in Fig. 3. The lengths of such segments are not equal, and more
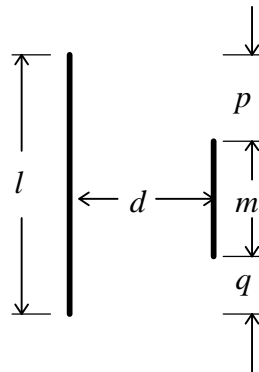

Fig. 4. Layout of non-equal length current filaments.

complicated formulas may be derived for such a case [15] [10]. Alternatively, the GMD of non-equal length conductors can be written in terms of equation (2). For instance, by symmetry arguments [15], for the non-equal length segments shown in Fig. 4, the appropriate equation is a combination of three equal length filaments

$$2M = M(m+p,d) + M(m+q,d) - M(p,d) - M(q,d) \qquad (13)$$

where $M(l,d)$ is given by equation (2).

For non-parallel conductors, the concept of GMD may be used but equation (4) becomes difficult to evaluate in closed-form. Since segments which couple most strongly tend to be parallel and closely spaced in a typical spiral, whereas non-parallel segments tend to be distant, we may assume that the magnetic field generated by such segments is equivalent to the magnetic field generated by a current filament flowing through the center of such conductors. With this approximation, the mutual inductance between infinitesimally thin filaments in arbitrary geometric relations to one another may be found using Neuman's formula or other techniques and such formulas appear in [15]. This approximation improves if we divide the cross-section of a conductor into many sub-sections to obtain the frequency-dependent current distribution [14].

4.2. High Frequency Current Constriction and Proximity Effects

As discussed in section 2.1, the current distribution at high frequency ceases to be uniform through the cross-section of the conductor segments and hence the GMD approximation fails at high frequency. The non-uniformity in the current distribution is not only due to the skin effect, but also due to proximity effects of neighboring current segments. Hence, although many past authors [16] have analyzed and developed closed-form equations for current constriction in an isolated conductor, these results are not directly applicable to the spiral inductor due to proximity effects.

In [11] a nice technique is developed to handle this problem without abandoning the closed-form equations already developed in section 2.2. In essence, as shown in equation (2.12), the current distribution in the conductor can be approximated in a step-

wise fashion by breaking up each segment into sub-segments. Although this technique is general and accurate, it is computationally expensive. Consider a typical 10-sided spiral with 10 turns as an example. Such a spiral has 100 segments, and if we were to further divide each segment into 5 parallel segments, this would involve 500 segments, and a corresponding 500×500 matrix inversion. To alleviate the demand on computational resources, we will assume that the segment current distribution is only influenced by a small set of neighboring segments. For a typical planar spiral, this might involve only two neighboring segments.

We re-derive the results presented in [11] with this approximation in mind. For a set of N segments, let the (i,j) segment represent the jth sub-segment of segment i and let N_i denote the number of such sub-segments in segment i. Let I_{ij} be the current in the (i,j) segment, and let I_i be the total current in segment i. With this notation, the voltage across the (i,j) segment is given by

$$V_{ij} = \sum_{k=0}^{N} \sum_{m=1}^{N_k} (r_{ij} \boldsymbol{d}_{ki} \boldsymbol{d}_{jm} + jwL_{ij,km})I_{km} \tag{14}$$

In the above equation r_{ij} is the resistance of the (i,j) conductor, $\boldsymbol{d}_{ij}$ is the Kronecker delta-function, and $L_{ij,km}$ is the mutual inductance between sub-segments (i,j) and (k,m). Let C_i denote the set of segments in the neighborhood of segment i, or the set of segments which influence the current distribution of segment i [17]. Equation (14) may be broken up as follows

$$V_{ij} = V_{ij}^{L} + V_{ij}^{G} = \sum_{k \in C_i} \sum_{m=1}^{N_k} Z_{ij,km} I_{km} + \sum_{k \notin C_i} jwL_{ik} I_k \tag{15}$$

Inverting the first term corresponding to the local voltage at segment (i,j) we obtain

$$I_{ij} = \sum_{k \in C_i} \sum_{m=1}^{N_k} Y_{ij,km} V_{km}^{L} \tag{16}$$

The total current in segment i is given by

$$I_i = \sum_{j=1}^{N_i} I_{ij} = \sum_{k \in C_i} \sum_{j=1}^{N_i} \sum_{m=1}^{N_k} Y_{ij,km} V_{km}^{L} \tag{17}$$

If we make the reasonable assumption that the voltage across each sub-segment (i,j) is independent of the index j (as was done in [11]), then (17) becomes

$$I_i = \sum_{k \in C_i} V_{km}^L \sum_{j=1}^{N_i} \sum_{m=1}^{N_k} Y_{ij,km} = \sum_{k \in C_i} V_{km}^L Y_{ik}^L \tag{18}$$

Equation (15) may be rewritten as

$$V_i = \sum_{k \in C_i} Z_{ik}^L I_k + \sum_{k \notin C_i} j\boldsymbol{w} L_{ik} I_k \tag{19}$$

Repeating for all i, one generates the desired matrix equation. The above technique involves one matrix inversion going from equation (15) to equation (16), and another matrix inversion of reduced order going from (18) to (19). The latter matrix inversion can be neglected, since the matrix is small. Assuming matrix inversion is the most computationally intensive operation, and that it is done $O(n^3)$, whereas the original technique presented in [11] is $O[(n{\times}p)^3]$, where n is the total number of segments and p is the average number of sub-segments, this technique is $O[n{\times}(q{\times}p)^3]$, where q is one plus the average number of neighbors for each segment. Hence this technique is n^2/q^3 faster and demands n^2/q^2 less memory to store the matrix. For the example given earlier, a 10-sided 10-turn spiral, with two neighbors and five sub-segments per segment, this means this technique is 370 times faster, and more than 1000 times less memory intensive.

Chapter 5: Capacitance and Substrate Loss Matrix Calculation

Although undesirable, all passive devices on the Si substrate suffer from substrate effects. The inherent capacitance between metal segments and the substrate leads to self-resonance at higher frequencies. After self-resonance, the inductors and transformers appear capacitive and fail to function as inductors. Hence, the highest frequency of operation is limited. Also, due to the finite conductivity of the substrate layers beneath the inductors and transformers, currents are induced in the substrate electrically and magnetically. These currents act as an important additional loss mechanism which limits the frequency of operation and the quality factor at high frequencies.

5.1 Capacitance Matrix and Approximations

In chapter 4 we found the GMD approximation to be very useful, as it allows one to bypass equation (4.1). The approximation lies in the assumption that the current distribution is uniform across the cross-section of the conductor. While this approximation is true at low frequency, it fails at high frequency due to current constriction and proximity effects. But as discussed before, we can always partition the cross-section into uniform current sections, as in equation (2.12), to approximate the physics at higher frequency.

Although the same approximation is used for the capacitance calculation, the partitioning of the segments into constant charge sections requires a lot more divisions to retain sufficient accuracy. This is due to the edge effects which cause high charge density at the edges of the conductors and large charge density variation near the edges. Non-uniform segment divisions help, but the basic problem remains. In addition, edge effects are important even for calculating capacitance at low frequency whereas current constriction and proximity effects are only important at higher frequency.

The substrate and coupling capacitance can be estimated using two dimensional approximations. Much work has been done in determining the capacitance of coupled

transmission lines in even and odd mode. The classic work of [18] gives closed form relations for these capacitors, but can involve lengthy numerical calculations. The work of [19] gives empirical closed-form equations which are suitable for computer applications. For most cases, the capacitance matrix can be approximated by a band-matrix by considering only the nearest neighbors in the coupling problem. This can be used to simplify the matrix inversion.

For an arbitrary arrangement of conductors, empirical methods or numerical methods must be employed. For instance, in [20] empirical formulas appear which allow one to find the capacitance matrix very quickly. Three dimensional numerical techniques, on the other hand, are computationally expensive. If the problem is constrained to two dimensions, fast numerical techniques are available. One such technique is the Method of Pipes [21]. In this finite-element technique, the electrostatic integral equations are developed with the edge effects in mind, necessitating fewer divisions at the edges of conductors.

The biggest drawback to many of these techniques is that they avoid the important effects of the conductive substrate. Pairs of segments not only couple through the oxide, but also through the conductive substrate. This can be represented as a lossy capacitor. Depending on the frequency of operation, the substrate coupling can be significant. Of course, it is of paramount importance to include the substrate loss of the capacitance to substrate. Many previous papers have assumed this resistance to be constant, an approximation which fails at high frequency. Due to displacement current in the substrate, the effective substrate impedance is a function of frequency. For an accurate characterization of these effects, (2.16) must be solved. A full treatment of the substrate problem follows.

5.2. Derivation of the Multi-Layer Green Function

To derive the electrostatic Green function in a multi-layer substrate, consider a point charge placed at (x',y',z') in layer k as shown in Fig. 1. The Green function must satisfy Poisson's equation in layer j

$$\nabla^2 G(x,y,z,x',y',z') = \frac{-\boldsymbol{d}(x-x')\boldsymbol{d}(y-y')\boldsymbol{d}(z-z')}{\boldsymbol{e}_k} \tag{1}$$

where we assume that layer k has a uniform permittivity of $\boldsymbol{e}_k$. Let $G = X(x,x')Y(y,y')Z'(z,z')$ in the above equations thus resulting in

$$YZ'\frac{d^2X}{dx^2} + Z'X\frac{d^2Y}{dy^2} + XY\frac{d^2Z'}{dz^2} = -\frac{\boldsymbol{d}(x-x')\boldsymbol{d}(y-y')\boldsymbol{d}(z-z')}{\boldsymbol{e}_k} \tag{2}$$

Assume $X = \cos[\frac{m_1\boldsymbol{p}x}{a}]$; $Y = \cos[\frac{n_1\boldsymbol{p}y}{b}]$ in order to satisfy the boundary condition of zero normal E-field on the side walls. Making these substitutions results

$$\sum_{m_1=0}^{\infty}\sum_{n_1=0}^{\infty}\cos[\frac{m_1\boldsymbol{p}x}{a}]\cos[\frac{n_1\boldsymbol{p}y}{b}]\left[\frac{d^2Z'}{dz^2} - \left(\left(\frac{m_1\boldsymbol{p}}{a}\right)^2 + \left(\frac{n_1\boldsymbol{p}}{b}\right)^2\right)Z'\right] = -\frac{\boldsymbol{d}(x-x')\boldsymbol{d}(y-y')\boldsymbol{d}(z-z')}{\boldsymbol{e}_k}$$

$$\tag{3}$$
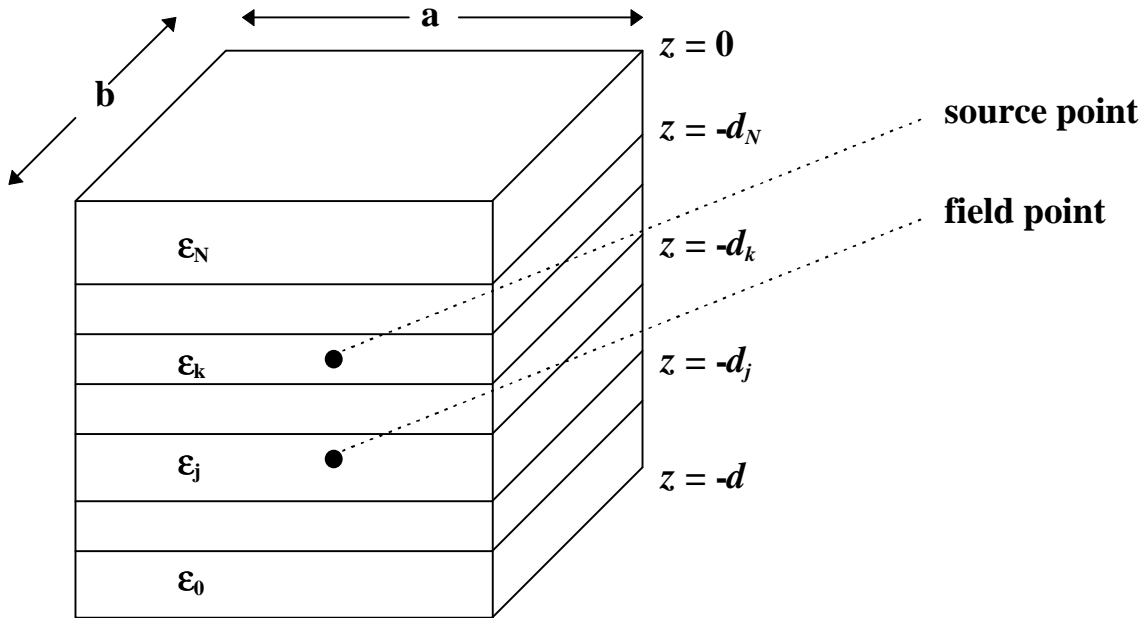
Fig. 1. Geometry of Multi-Layer Substrate.

By multiplying the above equations by $\cos[\frac{m\boldsymbol{p}x}{a}]\cos[\frac{n\boldsymbol{p}y}{b}]$ and by integrating over x and y chip dimensions we get

$$\frac{ab}{4}\left(\frac{d^2 Z'}{dz^2} - \left(\left(\frac{m\boldsymbol{p}}{a}\right)^2 + \left(\frac{n\boldsymbol{p}}{b}\right)\right)Z'\right) = -\frac{\boldsymbol{d}(z-z')}{\boldsymbol{e}_k}\cos[\frac{m\boldsymbol{p}x'}{a}]\cos[\frac{n\boldsymbol{p}y'}{b}] \qquad (4)$$

By defining $Z'(z,z') = Z(z,z')\cos[\frac{m\boldsymbol{p}x'}{a}]\cos[\frac{n\boldsymbol{p}y'}{b}]$ and substituting in the above equation we get a simple second-order differential equation

$$\frac{ab}{4}\left(\frac{d^2 Z}{dz^2} - \boldsymbol{g}_{mn}^2 Z\right) = -\frac{\boldsymbol{d}(z-z')}{\boldsymbol{e}_k} \qquad (5)$$

where $\boldsymbol{g}_{mn} = \sqrt{(\frac{m\boldsymbol{p}}{a})^2 + (\frac{n\boldsymbol{p}}{b})^2}$. For $z \neq z'$ the above equation has the general solution

$$Z = \boldsymbol{b}\sinh[\boldsymbol{g}_{mn}(d+z)] + \Gamma\cosh[\boldsymbol{g}_{mn}(d+z)] \qquad (6)$$

Hence, in each layer, the solution must be of the above form. In particular, in layer k the solution is of the form

$$Z_k^{u,l} = (\boldsymbol{b}_k^{u,l}\sinh[\boldsymbol{g}_{mn}(d+z)] + \Gamma_k^{u,l}\cosh[\boldsymbol{g}_{mn}(d+z)]) f_k^{u,l}(z') \qquad (7.a,7.b)$$

where the superscript u and l distinguish between the upper and lower solutions, depending if the observation point is above or below the point charge. The potential must be continuous at $z = z'$, and the first derivative discontinuity can be found by integrating equation (5) for $m,n > 0$.

$$Z_k^l(z') = Z_k^u(z') \qquad \left.\frac{dZ_k}{dz}\right|_{z'-d}^{z'+d} = -\frac{4}{ab\boldsymbol{e}_k} \qquad (8.a,8.b)$$

Using these two conditions, one can solve for the z' dependence of the potential

$$f_k^{u,l}(z') = \frac{4[\boldsymbol{b}_k^{u,l}\sinh(\boldsymbol{g}_{mn}(d+z')) + \Gamma_k^{u,l}\cosh(\boldsymbol{g}_{mn}(d+z'))]}{ab\boldsymbol{e}_k\boldsymbol{g}_{mn}(\Gamma_k^u\boldsymbol{b}_k^l - \Gamma_k^l\boldsymbol{b}_k^u)} \qquad (9.a,9.b)$$

In any other layer, the solution takes the same form as (7a) or (7b), depending on whether the observation layer j is above or below the point charge. Boundary conditions imply that the z' dependence must be the same as in the layer k. Hence, the most general solution for the z dependence of the potential is

$$Z_{j,k}^{u,l} = \frac{4}{ab\,e_k g_{mn}} \frac{(b_j^{u,l} \tanh J_f + \Gamma_j^{u,l})(b_k^{l,u} \tanh J_s + \Gamma_k^{l,u})}{(\Gamma_k^u b_k^l - \Gamma_k^l b_k^u)} \cosh J_f \cosh J_s \qquad (10.a,10.b)$$

where $J_{f,s} = g_{mn}(d - z_{f,s})$. Here we introduce the notation of the field point $z_f = z$ and the source point $z_s = z'$. The coefficients b_k and Γ_k still need to be determined. Even though we have two constants, only one is independent. By examining equation (7), it is clear that either b_k or Γ_k can be factored out and absorbed into the z' dependence. Due to the boundary condition at $z = -d$, i.e. zero potential at the back ground plane, we must choose $b_0 = 1, \Gamma_0 = 0$. Furthermore, for each adjacent layer, the following boundary conditions must hold at the interface

$$Z_k\big|_{z=-d_k} = Z_{k-1}\big|_{z=-d_k} \qquad\qquad e_k \frac{dZ_k}{dz}\bigg|_{z=-d_k} = e_{k-1} \frac{dZ_{k-1}}{dz}\bigg|_{z=-d_k} \qquad (11.a,11.b)$$

The above pair of equations lead to a recursion relation that adjacent layer coefficients must satisfy

$$\begin{pmatrix} b_k \\ \Gamma_k \end{pmatrix} = \begin{pmatrix} \frac{e_{k-1}}{e_k}\cosh^2 J_k - \sinh^2 J_k & (\frac{e_{k-1}}{e_k} - 1)\sinh J_k \cosh J_k \\ (1 - \frac{e_{k-1}}{e_k})(\frac{e_{k-1}}{e_k} - 1)\sinh J_k \cosh J_k & \cosh^2 J_k - \frac{e_{k-1}}{e_k}\sinh^2 J_k \end{pmatrix}\begin{pmatrix} b_{k-1} \\ \Gamma_{k-1} \end{pmatrix} \qquad (12)$$

By employing the above recursion, we can find the coefficients in any layer below the point charge layer k. Similarly, at the top layer, we impose the boundary condition

$$\frac{dZ_N}{dz}\bigg|_{z=-d_{N+1}=0} = 0 \qquad (13)$$

This implies that the top layer coefficient values are $b_N = 0, \Gamma_N = -\coth(g_{mn}d)$. Using the top layer coefficients, and using the inverse of (12), we can recurse downwards from the top layer to any layer above the point charge layer k. Hence, all unknowns have been determined. Therefore, for the case of $m,n > 0$ we have

$$G_{j,k}^{u,l} = \sum_{m=1}^{\infty}\sum_{n=1}^{\infty} \frac{4(b_j^{u,l} \tanh J_f + \Gamma_j^{u,l})(b_k^{l,u} \tanh J_s + \Gamma_k^{l,u})}{ab\,e_k g_{mn}(\Gamma_k^u b_k^l - \Gamma_k^l b_k^u)} \cosh J_f \cosh J_s \cos\frac{m p x}{a} \cos\frac{n p y}{b} \cos\frac{n p x'}{a} \cos\frac{n p y'}{b}$$

$$(14)$$

For the case $m=0$, $n>0$, or ($n=0$, $m>0$) the form of (14) remains the same except the factor 4 changes to 2 and we have a single summation instead of a double sum. For the case $m=n=0$, the original differential equation (5) has the general solution

$Z_k = B_k z + G_k$. Applying boundary conditions to adjacent layers results in the following recursion relations

$$B_j = \frac{e_{j-1}}{e_j} B_{j-1}$$

$$G_j = (\frac{e_{j-1}}{e_j} - 1) d_j B_{j-1} + G_{j-1} \qquad (15.a, 15.b)$$

To satisfy boundary conditions at the back-plane, we have $B_0^l = 1$, $G_0^l = d$. To satisfy the top-layer boundary condition (13), $B_N^u = 0 \Rightarrow B_j^u = 0 \ \forall j \in L_{upper}$ (upper layers). In addition, $G_j^u = G^u \ \forall j \in L_{upper}$. By applying the fact that the potential must be continuous across the point charge, and by integrating the differential equation (5) we find

$$Z_{j,k}^{\binom{l}{u}}(z, z') = \frac{B_j^{l,u}\begin{pmatrix} z \\ z' \end{pmatrix} + G_j^{l,u}}{ab e_k B_k^l} \qquad (16.a, 16.b)$$

The Green function derived above is represented as a double infinite series which converges slowly. In practical applications, we need a way to evaluate the Green function at many different points in the substrate, thus necessitating a technique for fast evaluation of (52). In [22] a technique of representing (14) as a Discrete Cosine Transform (DCT) is shown. We will use the same technique, and for continuity we will summarize the work of [22]. We begin by integrating the Green function over the surface of a contact. Equation (2.16) becomes:

$$\overline{f}_i = \frac{Q_j}{S_i S_j} \iint_{S_j S_i} G_{i,j} dS_j dS_i \qquad (17)$$

To find $p_{i,j} = \overline{f}_i / Q_j$, we integrate (14) and (16) over the surface of contacts i and j with coordinates given in Fig. 2. This results in

$$p_{i,j} = \frac{(B_i^{l,u}\{z,z'\} + G_i^{l,u})}{ab e_j B_j^l} + \sum_{m=1}^{\infty} \sum_{n=1}^{\infty} k_{mn,ij} C_{mn} \frac{a^2 b^2}{m^2 n^2 \boldsymbol{p}^4} \left[\frac{(\sin(m\boldsymbol{p} \frac{a_2}{a}) - \sin(m\boldsymbol{p} \frac{a_1}{a})))}{(a_2 - a_1)} \right.$$
$$\left. \frac{(\sin(m\boldsymbol{p} \frac{a_4}{a}) - \sin(m\boldsymbol{p} \frac{a_3}{a}))}{(a_4 - a_3)} \frac{(\sin(m\boldsymbol{p} \frac{b_2}{b}) - \sin(m\boldsymbol{p} \frac{b_1}{b}))}{(b_2 - b_1)} \frac{(\sin(m\boldsymbol{p} \frac{b_4}{b}) - \sin(m\boldsymbol{p} \frac{b_3}{b}))}{(b_4 - b_3)} \right] \qquad (18)$$

in the above equation $C_{00} = 0$, $C_{m0} = C_{0n} = 2$, and $C_{mn} = 4 \, \forall \, m,n > 0$. And

$$k_{mn,ij} = \frac{1}{ab\, \mathbf{e}_k \mathbf{g}_{mn}} \frac{(\mathbf{b}_i^{u,l} \tanh \mathbf{J}_f + \Gamma_i^{u,l})(\mathbf{b}_j^{l,u} \tanh \mathbf{J}_s + \Gamma_j^{l,u})}{(\Gamma_j^u \mathbf{b}_j^l - \Gamma_j^l \mathbf{b}_j^u)} \cosh \mathbf{J}_f \cosh \mathbf{J}_s \tag{19}$$

where the subscript s denotes the source point (with z coordinate of the contact in layer j), and the subscript f denotes the field point (with z coordinate of the contact in layer i).

By using the identity

$$\sin(m\mathbf{p} \tfrac{a_i}{a}) \sin(m\mathbf{p} \tfrac{a_j}{a}) = \tfrac{1}{2}(\cos(m\mathbf{p} \tfrac{a_i - a_j}{a}) - \cos(m\mathbf{p} \tfrac{a_i + a_j}{a})) \tag{20}$$

equation (21) can be cast into a sum of 64 terms in the form

$$\sum_{m=0}^{\infty} \sum_{n=0}^{\infty} x_{mn} \cos(m\mathbf{p} \tfrac{a_{1,2} \pm a_{3,4}}{a}) \cos(n\mathbf{p} \tfrac{b_{1,2} \pm b_{3,4}}{b}) \tag{21}$$

where

$$x_{mn} = \frac{a^2 b^2}{m^2 n^2 \mathbf{p}^4} k_{mn} C_{mn} \tag{22}$$

If we discretize the substrate space in the x-y directions, and represent the coordinates of the contacts as ratios of integers such that

$$\frac{a_k}{a} = \frac{p_k}{P}; \frac{b_k}{b} = \frac{q_k}{Q} \tag{23}$$

then (21) can be recast as

$$\sum_{m=0}^{P-1} \sum_{n=0}^{Q-1} x_{mn} \cos(m\mathbf{p} \tfrac{p_{1,2} \pm p_{3,4}}{P}) \cos(n\mathbf{p} \tfrac{q_{1,2} \pm q_{3,4}}{Q}) \tag{24}$$
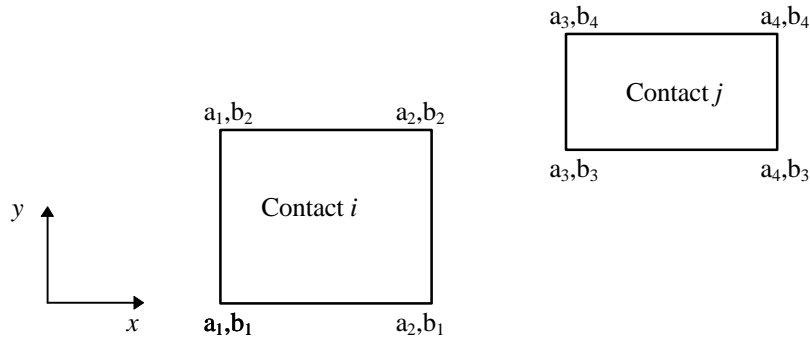
Fig. 2. Contact Coordinates

As (24) stands, it cannot be considered a DCT. However, using the following properties of the DCT allows one to compute (23).

$$X_{pq} = \sum_{m=0}^{P-1}\sum_{n=0}^{Q-1} x_{mn} \cos(m\boldsymbol{p}\,\tfrac{p}{P}) \cos(n\boldsymbol{p}\,\tfrac{q}{Q})$$

$$X_{2P-p,q} = X_{p,2Q-q} = X_{2P-p,2Q-q} = X_{p,q}$$

(25)

The Green function can therefore be computed rapidly by employing an FFT to compute the DCT.

The following list summarizes our algorithm for extracting the substrate parasitics.

A. For A Given Technology

- Input: Substrate layer data (thickness and dielectric constant and resistivity)
- Input: Metal layer z-coordinates
- For each pair of metal layers i and j, compute the Green function using the DCT method and store results. Due to symmetry of the Green function, for N_m metal layers, this requires $N_m(N_m+1)/2$ DCTs.

B. For A Given Layout

- Input: Contact x, y, z coordinates
- Form matrix [P] by accessing DCT of the Green functions
- Invert [P] matrix using LU factorization
- Form impedance matrix

Step A need only be done once for a given technology. This saves computation time since step A can be computationally expensive. For three metal layers, 6 2D DCTs need to be performed. Using the FFT, this operation is $O(p^2 \log p^2)$ where p represents the accuracy required. For a typical substrate dimension of $1024\mu m \times 1024\mu m$, a 512×512 DCT suffices. This sets the minimum metal trace width at $2\mu m$. Once step A is performed, step B uses the pre-computed Green functions to build the p-matrix. In other words, computation time is dominated by $O(n^3)$ where n represents the number of

contacts, not the DCT size. Although the accuracy of the method depends on the grid size of the DCT, this only affects step A, which is performed once, and not step B, which is performed many times.

5.3 Implementation of Numerically Stable Green Function

Although the derivation of section 5.2 is straightforward, the actual numerical implementation poses many problems. For large values of n and m, and deep substrate contacts, $\tanh J \to 1$ and $\cosh J \to \infty$. Furthermore, for each term $(\tanh J + \Gamma / b)$, the ratio $\Gamma / b \to -1$ so that the numerator factors of equation (10) approach zero. The denominator of (10) also approaches zero. The product of the ratio and the hyperbolic factors must converge to zero as a whole, due to the physical nature of the solution, but with finite precision it is very difficult to accurately calculate equation (10). The above equations, though, may be recast into more numerically stable forms as follows. We begin by rearranging equation (10a)

$$\left(\frac{(\boldsymbol{b}_j^u \tanh J_f + \Gamma_j^u)}{(\boldsymbol{b}_k^u \tanh J_f + \Gamma_k^u)}\right)\left(\frac{(\boldsymbol{b}_k^u \tanh J_f + \Gamma_k^u)(\boldsymbol{b}_k^l \tanh J_s + \Gamma_k^l)}{\Gamma_k^u \boldsymbol{b}_k^l - \Gamma_k^l \boldsymbol{b}_k^u}\cosh J_f \cosh J_s\right)$$

(26)

Notice that the we have separated the equations into a factor with only the source layer k and a factor involving an upper recursion of j,k. We define $r_k^l = \dfrac{\Gamma_k^l}{\boldsymbol{b}_k^l}, r_k^u = \dfrac{\boldsymbol{b}_k^u}{\Gamma_k^u}$ to simplify notation. We also rewrite (12) as follows

$$\begin{pmatrix}\boldsymbol{b}_k^l \\ \Gamma_k^l\end{pmatrix} = \cosh^2 J_k \begin{pmatrix} \frac{\boldsymbol{e}_{k-1}}{\boldsymbol{e}_k} - \tanh^2 J_k & (\frac{\boldsymbol{e}_{k-1}}{\boldsymbol{e}_k} - 1)\tanh J_k \\ (1 - \frac{\boldsymbol{e}_{k-1}}{\boldsymbol{e}_k})\tanh J_k & 1 - \frac{\boldsymbol{e}_{k-1}}{\boldsymbol{e}_k}\tanh^2 J_k \end{pmatrix}\begin{pmatrix}\boldsymbol{b}_{k-1}^l \\ \Gamma_{k-1}^l\end{pmatrix} = \cosh^2 J_k [A_k]\begin{pmatrix}\boldsymbol{b}_{k-1}^l \\ \Gamma_{k-1}^l\end{pmatrix}$$ (27)

$$\begin{pmatrix}\boldsymbol{b}_k^l \\ \Gamma_k^l\end{pmatrix} = \prod_{p=1}^k \cosh^2 J_p [A_p]\begin{pmatrix}\boldsymbol{b}_0^l \\ \Gamma_0^l\end{pmatrix}$$

(28)

From the above, we define new coefficients as follows

$$\begin{pmatrix} \tilde{\boldsymbol{b}}_k^l \\ \tilde{\Gamma}_k^l \end{pmatrix} = \prod_{p=1}^{k} [A_p] \begin{pmatrix} \tilde{\boldsymbol{b}}_0^l \\ \tilde{\Gamma}_0^l \end{pmatrix} \tag{29a}$$

and similarly

$$\begin{pmatrix} \tilde{\boldsymbol{b}}_k^u \\ \tilde{\Gamma}_k^u \end{pmatrix} = \prod_{p=k+1}^{N} [A_p^{-1}] \begin{pmatrix} \tilde{\boldsymbol{b}}_N^u \\ \tilde{\Gamma}_N^u \end{pmatrix} \tag{29b}$$

Using the above definitions, we rewrite (26) as

$$\left(\frac{(\boldsymbol{r}_k^u \tanh \boldsymbol{J}_f + 1)(\tanh \boldsymbol{J}_s + r_k^l)}{1 - \boldsymbol{r}_k^u r_k^l} \cosh \boldsymbol{J}_f \cosh \boldsymbol{J}_s \right) \left(\frac{(\tilde{\boldsymbol{b}}_j^u \tanh \boldsymbol{J}_f + \tilde{\Gamma}_j^u)}{(\tilde{\boldsymbol{b}}_k^u \tanh \boldsymbol{J}_f + \tilde{\Gamma}_k^u)} \right) \frac{1}{\prod\limits_{p=k+1}^{j} \cosh \boldsymbol{J}_p} \tag{30}$$

We will now treat each factor separately. We begin with the first factor in equation (30). The following recursion relations are derived from (12)

$$r_k^l = \frac{(1-q_k)\tanh \boldsymbol{J}_k + (1 - q_k \tanh^2 \boldsymbol{J}_k) r_{k-1}^l}{(q_k - \tanh^2 \boldsymbol{J}_k) + (q_k - 1)\tanh \boldsymbol{J}_k r_{k-1}^l} \tag{31}$$

$$\boldsymbol{r}_k^u = \frac{(p_k - \tanh^2 \boldsymbol{J}_{k+1})\boldsymbol{r}_{k+1}^u + (p_k - 1)\tanh \boldsymbol{J}_{k+1}}{(1 - p_k)\tanh \boldsymbol{J}_{k+1} \boldsymbol{r}_{k+1}^u + (1 - p_k \tanh^2 \boldsymbol{J}_{k+1})} \tag{32}$$

where $p_k = \dfrac{\boldsymbol{e}_{k+1}}{\boldsymbol{e}_k}, q_k = \dfrac{\boldsymbol{e}_{k-1}}{\boldsymbol{e}_k}$. Using (31) and (32), and substituting into the first factor of

(30) gives[1]

$$\frac{(R_{k-1}^l + q_k \tanh(\boldsymbol{J}_s - \boldsymbol{J}_k))(R_{k+1}^u + p_k \tanh(\boldsymbol{J}_f - \boldsymbol{J}_{k+1})}{q_k R_{k+1}^u - p_k R_{k-1}^l + \tanh(\boldsymbol{J}_k - \boldsymbol{J}_{k+1})(p_k q_k - R_{k+1}^u R_{k-1}^l)} \frac{\cosh(\boldsymbol{J}_s - \boldsymbol{J}_k)\cosh(\boldsymbol{J}_f - \boldsymbol{J}_{k+1})}{\cosh(\boldsymbol{J}_k - \boldsymbol{J}_{k+1})} \tag{33}$$

where

$$R_k^l = \frac{\tanh \boldsymbol{J}_{k+1} + r_k^l}{1 + \tanh \boldsymbol{J}_{k+1} r_k^l} \tag{34}$$

$$R_k^u = \frac{1 + \boldsymbol{r}_k^u \tanh \boldsymbol{J}_k}{\boldsymbol{r}_k^u + \tanh \boldsymbol{J}_{k+1}} \tag{35}$$

The above equations satisfy the following recursion relations and terminating conditions

---

[1] This follows after much algebra.

$$R_k^l = \frac{R_{k-1}^l + q_k \tanh(\boldsymbol{J}_{k+1} - \boldsymbol{J}_k)}{R_{k-1}^l \tanh(\boldsymbol{J}_{k+1} - \boldsymbol{J}_k) + q_k}, \; R_0^l = \tanh \boldsymbol{J}_1 \tag{36}$$

$$R_k^u = \frac{R_{k+1}^u + p_k \tanh(\boldsymbol{J}_k - \boldsymbol{J}_{k+1})}{R_{k+1}^u \tanh(\boldsymbol{J}_k - \boldsymbol{J}_{k+1}) + p_k}, \; R_N^u = \coth(\boldsymbol{J}_N - \boldsymbol{J}_{N+1}) \tag{37}$$

Using equations (36) and (37), (33) can be rewritten as

$$F_k^u = \frac{(R_k^l + \tanh(\boldsymbol{J}_s - \boldsymbol{J}_{k+1}))(R_k^u + \tanh(\boldsymbol{J}_f - \boldsymbol{J}_k)}{R_k^u - R_k^l + \tanh(\boldsymbol{J}_k - \boldsymbol{J}_{k+1})(R_k^u R_k^l - 1)} \frac{\cosh(\boldsymbol{J}_s - \boldsymbol{J}_{k+1})\cosh(\boldsymbol{J}_f - \boldsymbol{J}_k)}{\cosh(\boldsymbol{J}_k - \boldsymbol{J}_{k+1})} \tag{38}$$

The above equations may be evaluated in a numerically stable fashion since equations (34) and (35) are numerically stable as $\boldsymbol{J} \to \infty$. Equation (38) is valid for field points above the source point charge (upper case). However, due to the symmetry of equation (30), equation (38) can be rewritten for the lower case by inspection.

What remains is the second factor in equation (30). We may calculate this indirectly by using (34) and (35) as well. Rewriting (35) as a ratio:

$$R_k^u = \frac{N_k^u}{D_k^u} = \frac{(1 - \tanh \boldsymbol{J}_k \tanh \boldsymbol{J}_{k+1})(p_k \tanh(\boldsymbol{J}_k - \boldsymbol{J}_{k+1})D_{k+1} + N_{k+1})}{(1 - \tanh \boldsymbol{J}_k \tanh \boldsymbol{J}_{k+1})(\tanh(\boldsymbol{J}_k - \boldsymbol{J}_{k+1})N_{k+1} + p_k D_{k+1})} \tag{39}$$

The common factor is not canceled for a good reason. When calculating (35) as a ratio, this factor does not play an important role since it always cancels out. But if we wish to calculate N_k^u recursively, this factor is important. Let us observe that

$$N_k^u = (1 - \tanh \boldsymbol{J}_k \tanh \boldsymbol{J}_{k+1})(p_j \tanh(\boldsymbol{J}_k - \boldsymbol{J}_{k+1})D_{k+1} + N_{k+1}) = \prod_{p=k}^{N-1}(1 - \tanh \boldsymbol{J}_p \tanh \boldsymbol{J}_{p+1}) n_k^u \tag{40}$$

In equation (40) n_k^u is the numerator of (34), calculated recursively without the factor of $(1 - \tanh \boldsymbol{J}_p \tanh \boldsymbol{J}_{p+1})$. By using the above definitions, the first factor in equation (30) may be rewritten as

$$\frac{\tilde{n}_j^u}{\tilde{n}_k^u} \frac{\cosh(\boldsymbol{J}_f - \boldsymbol{J}_{j+1})}{\cosh(\boldsymbol{J}_f - \boldsymbol{J}_{k+1})} \frac{\cosh \boldsymbol{J}_{k+1}}{\cosh \boldsymbol{J}_{j+1}} \prod_{p=k+1}^{j} \frac{\cosh \boldsymbol{J}_p \cosh \boldsymbol{J}_{p+1}}{\cosh(\boldsymbol{J}_p - \boldsymbol{J}_{p+1})} \tag{41.a}$$

where $\tilde{n}_j^u$ is the numerator of (39) modified so that $\boldsymbol{J}_j = \boldsymbol{J}_f$. A similar analysis for the lower case gives

$$\frac{\tilde{n}_j^l}{\tilde{n}_k^l} \frac{\cosh(\boldsymbol{J}_f - \boldsymbol{J}_j)}{\cosh(\boldsymbol{J}_f - \boldsymbol{J}_k)} \frac{\cosh \boldsymbol{J}_k}{\cosh \boldsymbol{J}_j} \prod_{p=j}^{k-1} \frac{\cosh \boldsymbol{J}_p \cosh \boldsymbol{J}_{p+1}}{\cosh(\boldsymbol{J}_p - \boldsymbol{J}_{p+1})} \tag{41.b}$$

Utilizing the above results, the complete upper Green function z dependence can be rewritten as

$$Z_{j,k}^u = \frac{4 \, F_k^u(z_f, z_s)}{ab\boldsymbol{e}_k \boldsymbol{g}_{mn}} \frac{\tilde{n}_j^u}{\tilde{n}_k^u} \frac{\cosh(\boldsymbol{J}_f - \boldsymbol{J}_{j+1})}{\cosh(\boldsymbol{J}_f - \boldsymbol{J}_{k+1})} \frac{\cosh \boldsymbol{J}_k}{\cosh \boldsymbol{J}_{j+1}} \times$$
$$\prod_{p=k}^{j} \frac{\cosh \boldsymbol{J}_p \cosh \boldsymbol{J}_{p+1}}{\cosh(\boldsymbol{J}_p - \boldsymbol{J}_{p+1})} \cosh(\boldsymbol{J}_s - \boldsymbol{J}_{k+1}) \cosh(\boldsymbol{J}_f - \boldsymbol{J}_k) \tag{42.a}$$

and the lower case can be written as

$$Z_{j,k}^l = \frac{4 \, F_k^l(z_f, z_s)}{ab\boldsymbol{e}_k \boldsymbol{g}_{mn}} \frac{\tilde{n}_j^l}{\tilde{n}_k^l} \frac{\cosh(\boldsymbol{J}_f - \boldsymbol{J}_j)}{\cosh(\boldsymbol{J}_f - \boldsymbol{J}_k)} \frac{\cosh \boldsymbol{J}_j}{\cosh \boldsymbol{J}_{k+1}} \times$$
$$\prod_{p=j}^{k} \frac{\cosh \boldsymbol{J}_p \cosh \boldsymbol{J}_{p+1}}{\cosh(\boldsymbol{J}_p - \boldsymbol{J}_{p+1})} \cosh(\boldsymbol{J}_f - \boldsymbol{J}_{k+1}) \cosh(\boldsymbol{J}_s - \boldsymbol{J}_k) \tag{42.b}$$

The above equations are numerically stable and may be used to implement the algorithm presented in section 5.2.

5.4 IC-Interconnect as an Example

In this section, we illustrate the above described techniques with examples. We start with the simplest possible example of a single metal contact in two hypothetical Si IC processes. The first process, shown in Fig. 3, consists of a thick highly doped substrate and a thin lightly doped epi (such as a typical CMOS process). The second process,

R_{SH}=25Ω/sq	
$\boldsymbol{e}_{ox}$= 3.9	t = 1 μm
$\boldsymbol{e}_{ox}$= 3.9	t = 1 μm
$\boldsymbol{r}_{EPI}$=100 kΩ-μm	t = 5 μm
$\boldsymbol{r}_{SUB}$= 100 Ω-μm	t = 300μm

R_{SH}=25Ω/sq	
$\boldsymbol{e}_{ox}$= 3.9	t = 1 μm
$\boldsymbol{e}_{ox}$= 3.9	t = 1 μm
$\boldsymbol{r}_{EPI}$=500 Ω-μm	t = 1 μm
$\boldsymbol{r}_{SUB}$= 100 kΩ-μm	t = 300μm

Fig. 3. Lightly/Highly Doped Epi/Substrate   Fig. 4. Highly/Lightly Doped Epi/Substrate

shown in Fig. 4, consists of a thick lightly doped substrate and a thin highly doped surface layer (such as a buried layer in a BiCMOS process). The oxide thickness and metal sheet resistivity are the same in both processes. We use a metal contact with a length of 100 μm and a width of 10 μm located at approximately the center of a 256 μm × 256 μm chip.

Using the algorithm described in section 2, we compute the impedance of the contact. In our case, we subdivided the contact into 100 internal divisions. Figure 5 is a plot of the magnitude and phase of the contact impedance for the two processes. At increasingly higher frequency, the contact presents a lower impedance due to the capacitive nature of the substrate current injection. The contact has a lower impedance in the first process due to the highly doped bulk substrate layer. On the other hand, the impedance of the second process is very sensitive to the presence of a substrate tap[2]. As shown in Fig. 5, when a 10 μm × 10 μm substrate tap is located 30 μm away from the contact, the impedance drops to a value below that of process 1. The impedance drops
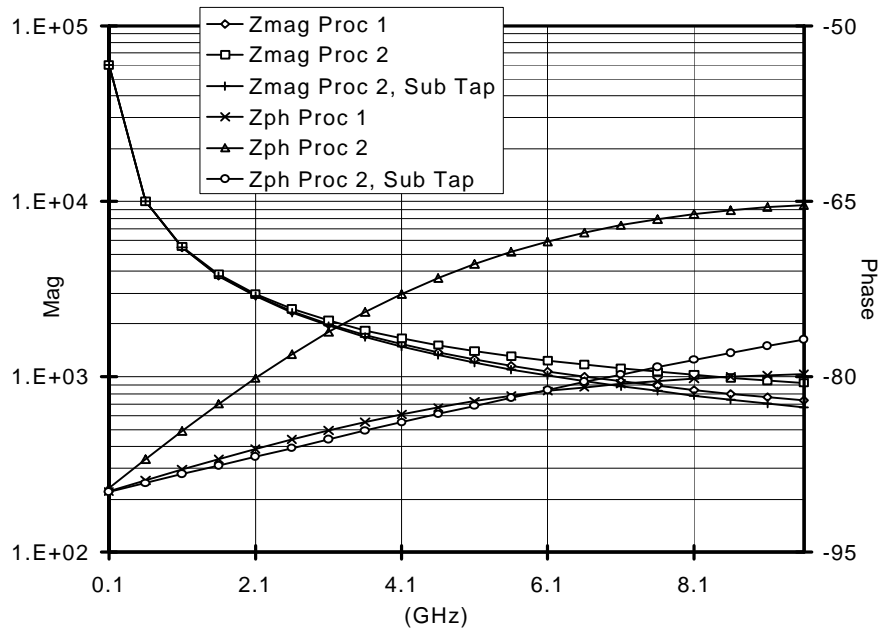
Fig. 5. Magnitude and Phase of Contact to Substrate Impedance for Processes 1 and 2

---

[2] A substrate tap is a metal contact to the surface of the substrate.
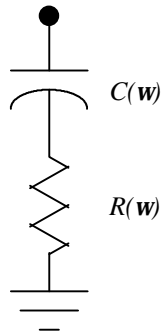
Fig. 6. Frequency Dependent Model of Contact
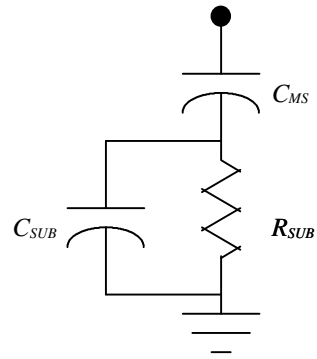
Fig. 7. Frequency Independent Model of Contact

since significant lateral current flows through the surface of the substrate. This indicates the importance of modeling the presence of a substrate tap in such a process. On the other hand, process 1 is not sensitive to the presence of the substrate tap since most current flows vertically through the surface epi layer.

Fig. 6 shows the extracted model, which is highly frequency-dependent. We can model the contact impedance with fixed capacitors and a resistor as shown in Fig. 7. This is the physical representation, with a fixed C_{MS} representing the metal to substrate
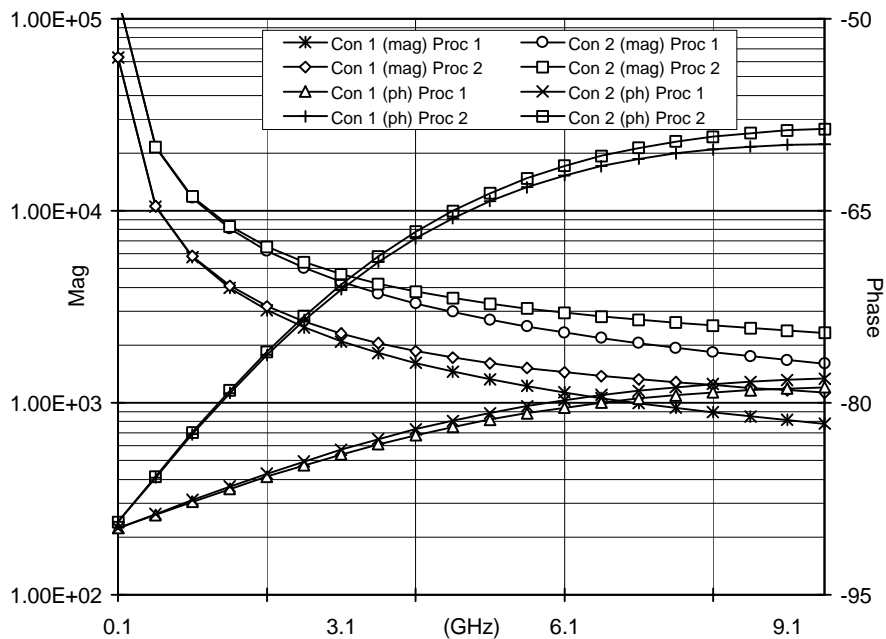
Fig. 8. Contact to Substrate Impedance For Two Contacts of Different Area
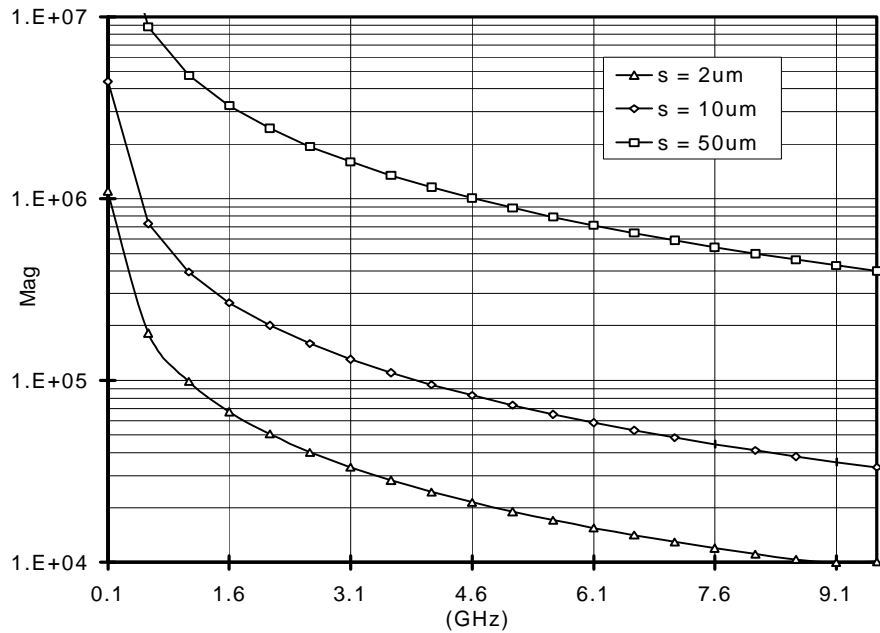
Fig. 9. Substrate Coupling Impedance for Process 1 for Different Contact Spacing Values

capacitance, and a fixed resistance R_{SUB} and capacitance C_{SUB} from the substrate to the ground plane. The agreement between the model and the previous simulation result is excellent.

Using the same simulation setup as described before, we examine the coupling impedance between two contacts. Two contacts are placed symmetrically around the center of the chip, one contact of length 100 μm and width 10 μm, the other contact of length 50 μm and width 10 μm. Three values of spacing are simulated: 2 μm, 5 μm, and 10 μm. Similar to the single contact case, the contact to substrate impedance is plotted in Fig. 8. For both processes, the larger contact naturally presents a lower impedance. The coupling impedance values are plotted in figures 9 and 10. Here we see significant differences. For the first process, Fig. 9 shows that the value of the spacing is very significant and the coupling impedance changes by orders of magnitude for different spacing values. For the second process, however, Fig. 10 shows that the contact impedance is not too sensitive to the spacing used. This is understandable since the second process coupling current flows laterally through surface, whereas in the first process lateral current flows through the bulk substrate.
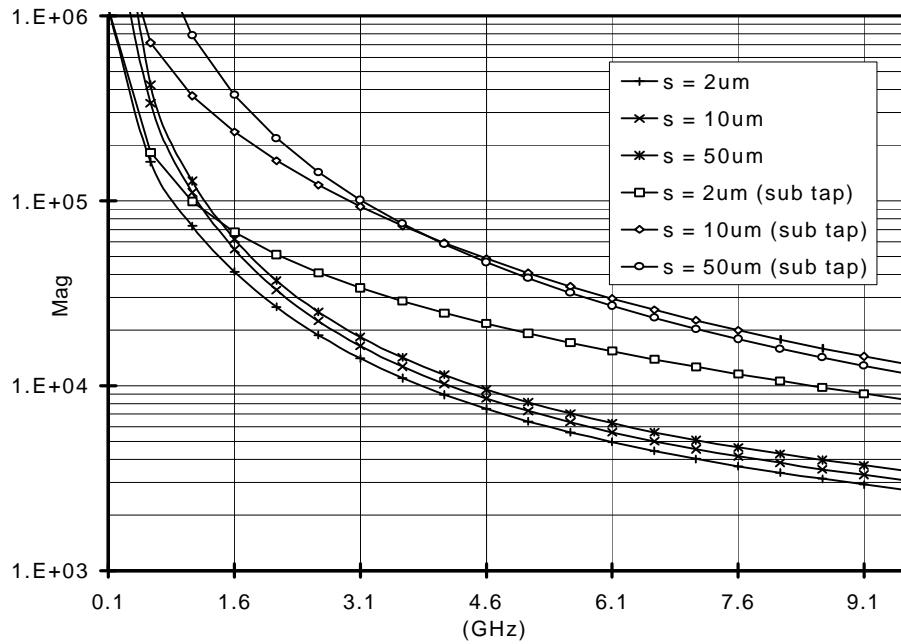
Fig. 10. Substrate Coupling Impedance for Process 2 for Different Contact Spacing Values

Fig. 10 also shows that the coupling impedance changes dramatically in the presence of a substrate tap placed between the contacts. As a result, a significant fraction of the lateral surface current flows to ground instead of to the other contact. The same isolating effect is not seen in the first process due to the highly resistive surface layer. Similar to before, frequency-independent circuits can be constructed to model the impedance over a wide-frequency range.

Chapter 6: Modeling

Since our inductance and capacitance matrix calculations are frequency dependent, our previous approach produces a frequency dependent model of the device. This is not a serious limitation since most RF circuits employing inductors and transformers in narrow-bands. On the other hand, enough situations arise in practice to warrant a frequency-independent model. On another front, measured data is often fit to frequency-independent models over a broad frequency range and this necessitates modeling the device with low-order circuits.

6.1 Equivalent Circuit of Planar Spiral

In the previous chapters we discussed how to generate two-port parameters as a function of frequency for a given spiral layout. Usually, the spiral inductor will be used in a larger circuit, with hundreds of other active and passive components. Hence, it is desirable to model the spiral two-port parameter with a low-order lumped circuit to reduce simulation time. In some cases, the y-parameters of the spiral can be utilized directly in the simulator; for the most part, however, it is more desirable to work with an equivalent circuit since this gives the designer more intuition about the performance of the circuit relative to the spiral inductor.

Fig. 1a shows a frequency independent model first proposed in [1] and Fig. 1b shows modifications to the circuit [2]. Most modifications model second order effects that increase the effective usable bandwidth of the model. For instance, a C_{BR} has been added to model the interwinding capacitance and to make the series inductance and resistance frequency dependent. Some authors [2] use a non-linear resistor to model skin/proximity effects. C_S represents displacement current in the substrate which makes the substrate impedance vary as a function of frequency. R_C is a substrate coupling resistor, which models the substrate coupling impedance.
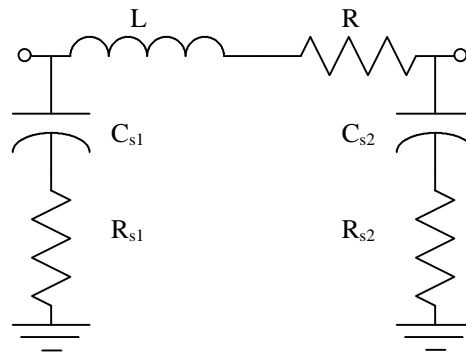
Fig. 1a. Traditional spiral inductor model.

Although the circuit of Fig. 1a may be derived physically at a single frequency from the two-port parameters, it is very difficult to physically derive models like Fig. 1b over a large frequency range. Usually optimization is used to minimize the least-square error between the two-port parameters of the two circuits. These circuits model the spiral well up to the first resonant frequency.

6.2 Equivalent Circuit of Multi-Level Spiral

To overcome the high losses intrinsic to Si spiral inductors, many authors [3][4] have reported utilizing processes with multiple metal layers to build inductors. Spirals on individual metal layers are interconnected by copious amounts of via connections, putting the spirals in shunt or in series. The purpose of making shunt connections is to increase the effective thickness of the metal conductor to thereby reduce the loss of the spiral. For
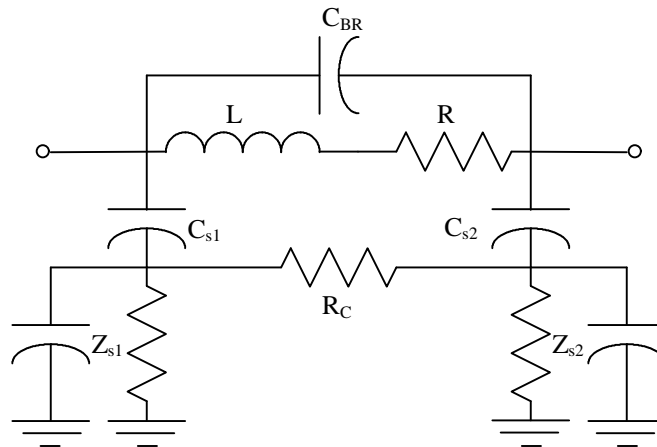
Fig. 1b. Modified spiral inductor model.

N metal layers with equal conductivity in shunt, the spiral loss at low frequency will drop by a factor of *N*. The inductance drops also, but since the metal-to-metal spirals are tightly coupled magnetically (k > 0.8), the loss in inductance is not substantial. Hence, the overall Q of the inductor increases.

Assuming perfect coupling as an upper bound, at low frequency the Q increases by a factor of *N*. The shunt connection combats high frequency losses due to current-constriction, since the multiple metal layers increase the available surface area for current to flow. The penalty is that the substrate admittance of the spiral increases since the spiral moves closer to the substrate with the lower metal layers. In addition, coupling capacitance increases. Hence, high-frequency Q suffers due to substrate loss.

Alternatively, the *N* spirals may be connected in series increasing the overall resistance and inductance of the spiral. The increase in resistance is more than a factor of *N* (assuming equal conductivity metal layers and some finite via resistance) whereas the inductance increases at a faster rate. For the ideal case of perfect coupling, the inductance increases by a factor N^2 (as in the case of discrete coil inductors). Hence, at low frequency, an upper bound on the Q increases is *N* for *N* metal layers, similar to the shunt connection. The series connection, however, suffers from high interwinding capacitance which lowers the self-resonant frequency substantially. This renders the series connection suitable for low-frequency small-area applications.

For both cases considered, modeling and analysis of the inductors become very important since the geometry has an adverse effect on the frequency response of the inductor. The analysis presented in chapter 3 is applicable, although many of the approximations are not. For instance, for the series connection capacitance is of utmost importance and must be computed accurately using the techniques of chapter 5. In addition, the simplified low frequency analysis of section 3.2 is no longer applicable, since we assumed operation far from self-resonance and negligible current flowing in the interwinding capacitance. For the shunt case, though, almost all of the analysis techniques

apply. In particular, the technique of section 3.1 can be used to model the parallel segments since this fits naturally into our earlier formulation.

The equivalent circuit for the shunt spiral is identical to the planar inductor. Special care is needed to calculate substrate capacitance/resistance since these effects are more important. The series inductor, though, is more difficult to model with simple circuits such as Fig. 1b. The reason is due to the lower self-resonance frequency and increased capacitance. These effects may be modeled by using two or three cascades of Fig. 1a with added coupling capacitors. Again, it is difficult to uniquely assign values to the model parameters, due to the unphysical nature of the modeling.

6.3 Equivalent Circuit of Transformers and Coupled Inductors

Similar to inductors, transformers find many important applications in a typical RF circuit. For example, transformer baluns aid in converting signals from differential to single-ended, and vice versa. In this way, they can be used to improve the gain of differential circuits which feed single-ended circuits [24]. In [25] a transformer is used as a low-noise feedback element to improve the performance of a LNA. Since inductance is a well controlled parameter (primarily determined by lithography), absolute inductance values are accurate to begin with, and inductor ratios are even more accurate. This allows inductors to be used as loads and as feedback elements. Other uses include filtering applications, tuned differential loads, and single-ended to balanced conversion, and narrow
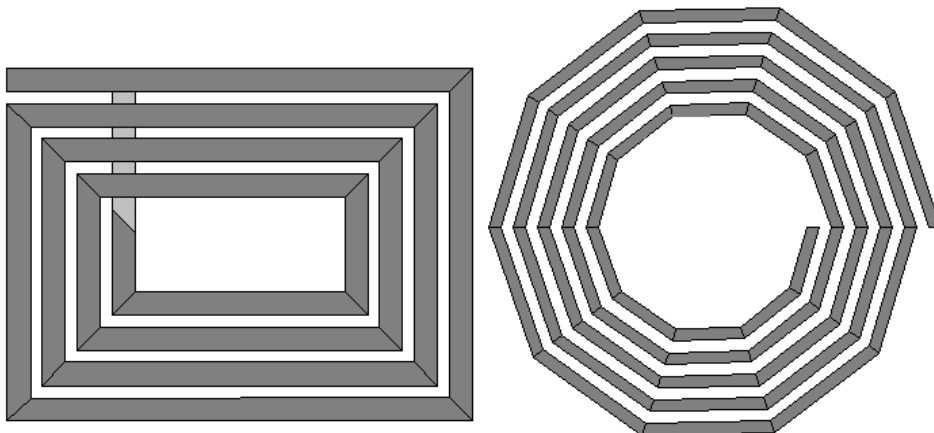
Fig. 2. Layout of two coupled spiral structures.
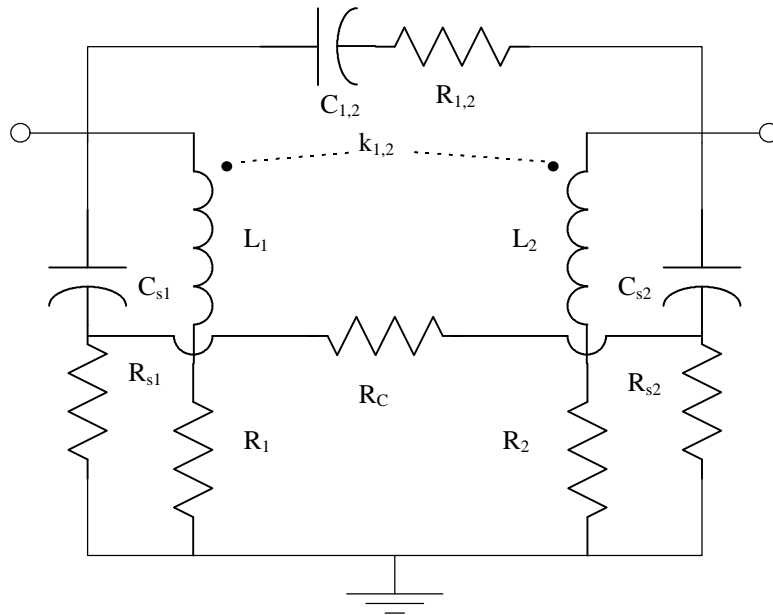
Fig. 3. Equivalent circuit model for two coupled spirals.

band impedance matching.

Most past researchers, however, have used transformer models derived from measurement, making it difficult to utilize a custom transformer prior to fabrication. Modeling of the spiral transformer is difficult since many second-order effects in the spiral analysis become first-order effects. This includes the interwinding coupling capacitance and the finite substrate coupling impedance.

We begin with the simplest case, that of coupled inductors. Assume that two spirals are placed on the Si substrate as shown in Fig. 2. Also assume that one side of each inductor is grounded. These inductors act like a loosely coupled transformer and may be modeled physically as shown in Fig. 3. This broadband equivalent circuit is derived by utilizing the calculations of chapter 3 to derive a lumped circuit representation at each frequency of interest. Through the use of optimization, the broadband model may be derived. In the broadband model R_c models the substrate coupling between the inductors. This is sensitive to the location of the substrate taps, as well as the condition of the back-plane of the Si substrate. Clearly, substrate taps placed between the spirals as well as a good back-plane ground help to isolate the inductors.
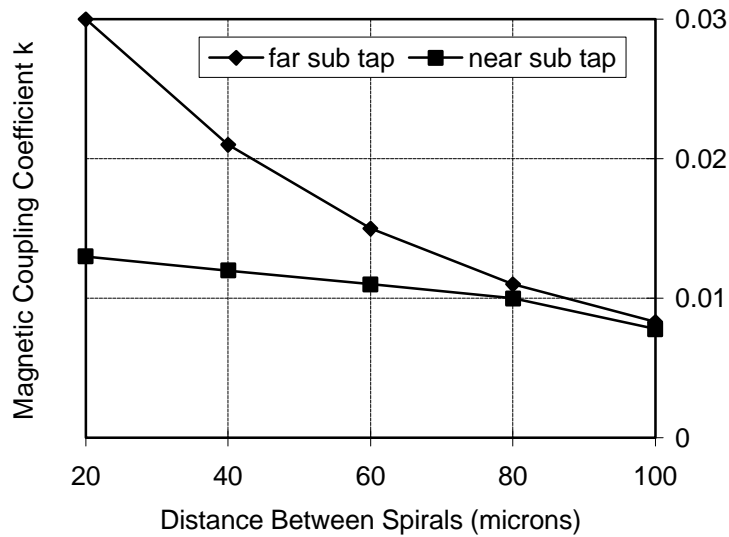
Fig. 4. Magnetic coupling coefficient for two coupled spirals as a function of distance between spirals.

Notice that the magnetic coupling coefficient k is very small for this arrangement of inductors. This remains true even as the spirals are placed in close proximity to one another. Fig. 4 is the computed plot of the effective k as a function of distance. Notice that k drops off very fast for distant spirals. Fig. 5 shows the magnitude of the coupling impedance for two different substrate tap placements. Whereas in the first case, a substrate tap is placed between the spirals, in the second case the substrate tap is placed a
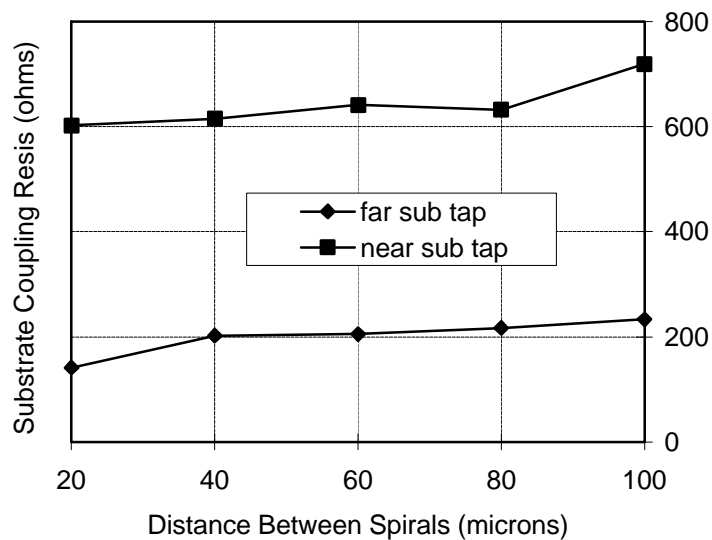
Fig. 5. Substrate coupling resistor for two coupled spirals as a function of distance between spirals.
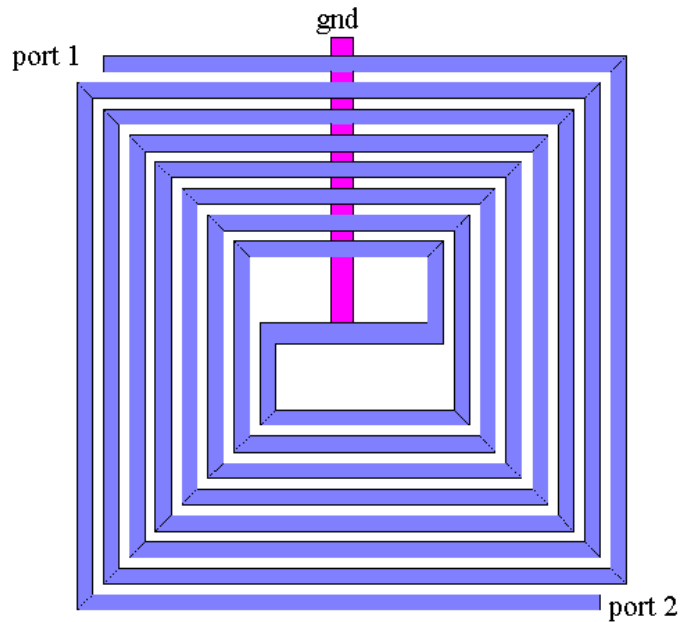
Fig. 6. Layout of planar transformer.

distance of 150 µm away from the spirals. It is evident that the placement of the substrate tap has an important effect on coupling.

Fig. 6 shows the layout of a typical spiral transformer. The transformer is realized simply as two spiral inductors wound together. Hence, we may calculate equivalent circuit parameters in a manner similar to before, and build equivalent circuits in exactly the same way. The coupling capacitance is especially important since it appears from one port of the transformer to the other and it is parasitic and dominant. For an isolated grounded spiral, the coupling capacitance is shunted by a much larger substrate capacitance and its effect on the inductance is second order. The equivalent broadband circuit is shown in Fig. 7a. This circuit may be transformed into the equivalent circuit of Fig. 7b [25][26], which utilizes an ideal transformer shunted by various parasitic elements.
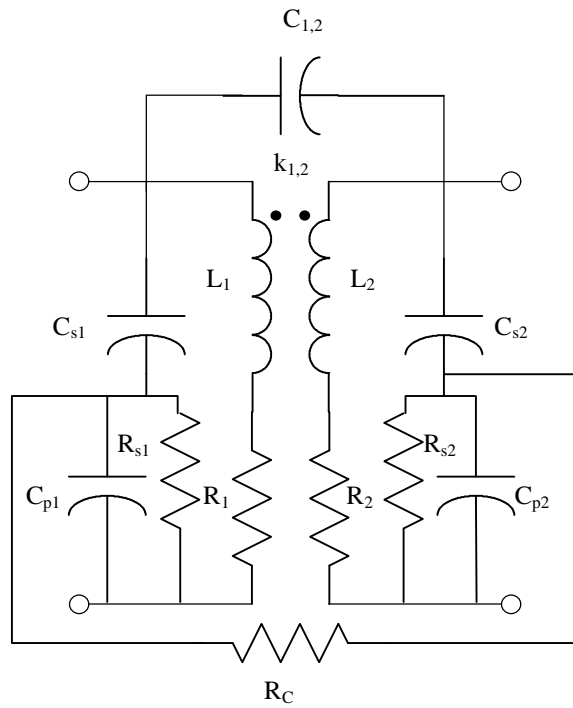
Fig. 7a. Equivalent circuit model for planar transformer.
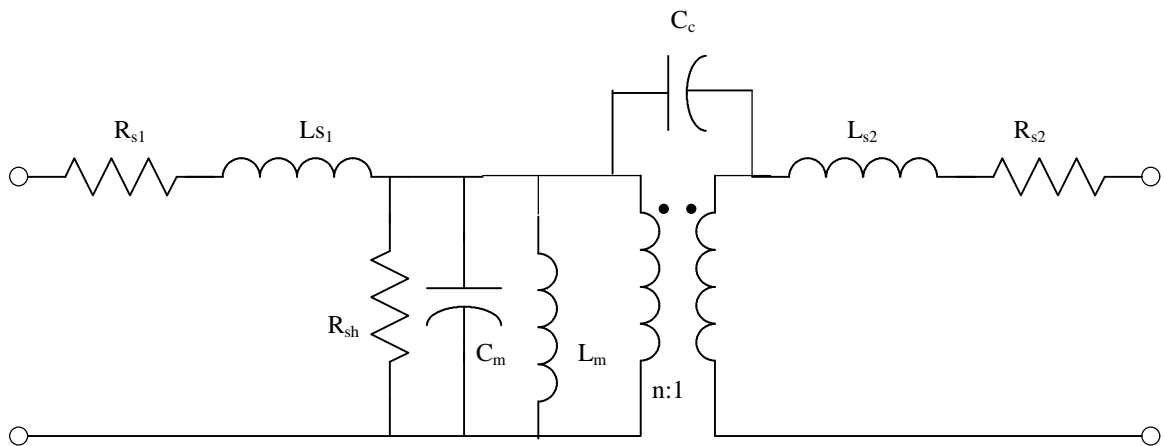
Fig. 7b. Equivalent circuit model for planar transformer with ideal transformer and parasitic elements.

Chapter 7: Optimization

In this chapter we pursue the optimal geometry and technology for the fabrication of inductors and transformers. While the word optimal is application dependent, invariably optimality depends in some way or another on the device quality factor. Hence, our optimization efforts will be biased in this direction.

7.1 Optimization of Technological Parameters

In this section, we consider optimizing the Si IC process in order to optimize the performance of inductors. At low-frequency, the dominant source of loss comes from the series loss of the spiral. A process utilizing thick metal [27], or high conductivity metal [2] can be utilized to improve the low-frequency performance of the inductors. At high frequency, the substrate loss limits the Q, and the substrate capacitance lowers the self-resonant frequency of the structure. Clearly, utilizing thicker oxide and lower permittivity dielectric helps to reduce the capacitance [7]. By increasing the self-resonant frequency, the substrate loss is also lowered. Alternatively, if special processing steps are taken, the spiral may be isolated from the substrate by etching away the oxide below the spiral and floating the inductor [6]. In addition to lowering the permittivity of the spiral capacitance, it also moves the spiral farther away from spiral. This increase in self-resonance allows one to design physically larger inductors, either to minimize loss or to attain a higher inductance value.

The substrate loss can be reduced by eliminating the substrate resistance. This can be done by either shorting out the substrate resistance or by open-circuiting it [22]. To short it out, one can place a high-conductivity conductor under the spiral, or alternatively place the spiral above a highly doped grounded layer. While this will reduce the substrate resistance value, it will have the deleterious effect of inducing substrate currents to flow. Recall that in chapter 4 this ground current was neglected in the inductance calculation. If this component is taken into account, its effect is to reduce the inductance of the spiral.

To understand this, consider a perfectly conducting ground layer. Using the method of images under quasi-static approximation, the ground current will mirror the substrate current, producing a magnetic emf in opposition to the spiral [28]. To combat this effect, one can place conductive strips in a grid fashion utilizing low conductance "open-circuit" spaces to minimize eddy currents. This is the approach taken by [35]. One must exercise caution, though, as the substrate shield might adversely affect the substrate coupling at high frequency due to the finite inductance in the ground. Also, the substrate shield must be sufficiently thick (thicker than the skin-depth in the material in question) to be effective at high frequency.

To increase the substrate resistance, one can utilize a lowly doped substrate. In the limit, the substrate becomes intrinsic and [29] has reported good performance with this substrate. As discussed in section 6.2, multiple metal layers can be used to improve inductor performance. Hence, IC processes with many metal layers can be advantageous. In summary, the ideal spiral inductor process is one with a thick low permittivity oxide isolating many thick highly conductive metal layers from a highly resistive substrate.

7.2 Optimization of Geometrical Parameters

Consider utilizing a typical Si IC process in the design of the inductor. A given design places constraints on the electrical parameters of the spiral. Typically, these constraints can be formulated as

$$
\begin{aligned}
&L_{\min} \leq L \leq L_{\max} \\
&R_{\min} \leq R \leq R_{\max} \qquad or \qquad \min[R] \\
&f_{res} \geq f_{\max} \\
&\max[Q]
\end{aligned}
\tag{1}
$$

While the designer typically places the strongest constraints on L, in RF choke applications it may be desirable to maximize L. The series loss, though, is usually parasitic and one wishes to minimize it. Nevertheless, some designs require a specific value for R. Ideally, one wishes to maximize the self-resonant frequency, but realistically one must live "close" to resonance due to the low self-resonant frequency of the structure. For the most

part, one wishes to maximize Q. Also, one wishes to place the frequency of maximum Q at the frequency of operation.

These electrical constraints map into corresponding geometric constraints. For a given typical spiral, as shown in Fig. 1.1, one must choose the parameters to satisfy the desired electrical constraints.

First, one has to decide on the geometry (square, circular, hexagon, etc.) or the number of sides p of the spiral polygon. Most past designs have utilized square spirals for simplicity, but square spirals are not necessarily optimal. For minimum loss, one would like to let p approach infinity, thus utilizing a circular spiral. In practice, a sufficiently large p, such as 30, closely approximates a circular spiral.

Given p, one can further change the spiral metal width w, the metal-to-metal spacing s, and the number of turns n. These parameters do not necessarily have to remain constant throughout the spiral either, or they may taper as a function of n. Of course, these parameters are not independent. Assuming that s and w are a function of n only, then the following approximate equation restricts the parameters space greatly

$$A_o = A_i + 2\sum_{j=1}^{n}(w_j + s_j)$$ (2)

In order to improve the low-frequency performance of the spiral of a given inductance, one must minimize the series loss of the spiral. This can be done by increasing w as much as possible. This requires more and more spiral area to achieve the desired inductance; this process is limited by the negative effects of the substrate loss, since increasing the spiral area increases the substrate injection in addition to lowering the self-resonant frequency. An optimum point exists at each frequency, and one can begin by finding the optimal area.

Next, consider the spacing s. Electrically, s controls the oxide coupling capacitance and the mutual magnetic coupling coefficient. But given that for most planar spirals the substrate capacitance is dominant, the bridging capacitance does not play an
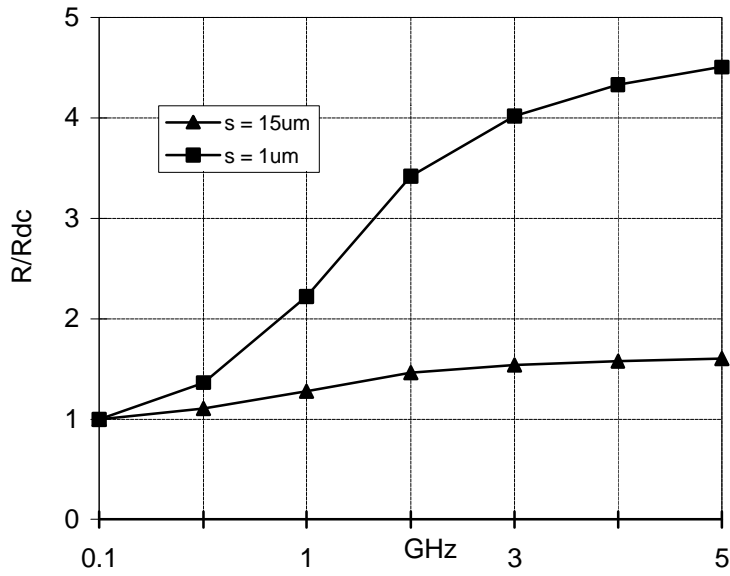
Fig. 1. Normalized spiral resistance as a function of frequency.

important role and hence may be ignored in the optimization. Typically, one chooses to minimize *s* up to a point where coupling capacitance becomes dominant. Minimizing *s* allows one to maximize mutual magnetic coupling. It also reduces loss by allowing wider metal line widths. But the value of *s* also affects current constriction. Hence, while at low frequency one usually uses the minimum spacing available to maximize magnetic coupling, at high frequency proximity effects favor a larger value of spacing [8]. This is illustrated in Fig. 1 where we plot the resistance of a typical spiral using two values of spacing. Similar considerations apply to the area of the spiral and the number of turns. At lower frequencies large areas allow wider metal widths to meet a given inductance at lower values of series resistance and therefore higher Q. But at high frequencies the Q is dominated by the substrate and smaller areas are favorable. This is doubly true for highly conductive substrates which suffer from eddy-current losses at high frequency [8].

Given A_o and minimum *s*, one can vary *w* and *n* to obtain the optimal Q at a particular frequency. Fig. 2 plots the optimum number of turns *n* as a function of outer length of a square spiral for different inductance values (the width *w* also varies). The analysis was performed at 2 GHz using a hypothetical BiCMOS process. This optimization is
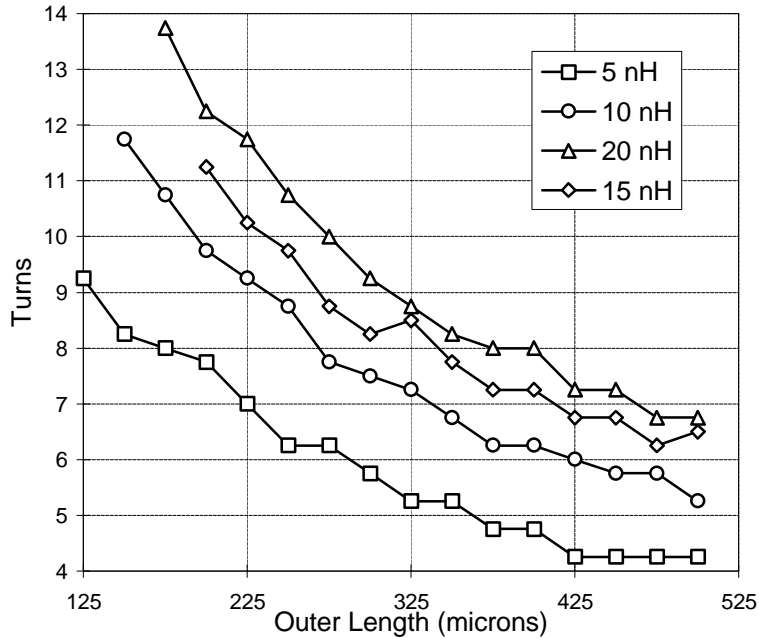
Fig. 2. Optimum spiral turns versus outer length for square spirals.

appropriately done using a computer program. Instead of considering every possible combination of (*n*,*w*,*s*), many heuristics can be used to restrict the parameter space. For instance, approximate closed-form formulas [30][31] may be used to estimate a range for *n* for a given *w* in order to achieve a particular value of inductance.

In the above discussion, we assumed that *w* does not vary as a function of *n*. This is not the optimal choice due to the intrinsic asymmetry of the spiral. This asymmetry becomes important at high frequency when proximity effects render the optimal width *w* position dependent. The inductance of the spiral is a weak function of *w*, whereas the loss is strongly dependent on *w*. By keeping the average width and length of the spiral constant, the inductance will not change significantly. To take advantage of this, one may taper the width of the spiral to optimize the Q.

7.2 A Custom CAD Tool for Spiral Design, Analysis, and Optimization

The techniques presented in this paper have been collected into *ASITIC* [32] (*A*nalysis and *S*imulation of *I*nductors and *T*ransformers for *IC*s), a user-friendly CAD tool designed to aid the RF circuit designer in designing, optimizing, and modeling of the spiral inductor. The tool is flexible, allowing the user to trade off between speed and accuracy. For example, to quickly search the parameters space of an inductor optimization problem, *ASITIC* uses low-accuracy high-speed techniques of chapter 3 to quickly confine the search space, then the local space is searched using more accurate techniques.

By working with the entire metal layout of the circuit at hand, *ASITIC* allows general magnetic and substrate coupling to be analyzed between different parts of the circuit. Parasitic metal extraction may also be performed, including the effects of the substrate, and the resulting SPICE file may be included in more accurate simulations. The final design of a spiral may be exported for final layout; this feature is convenient in the layout of complex geometry spirals (non-square spirals), since their hand-layout is time consuming, especially when changes are made to the geometry of the spiral.

Chapter 8: Experimental Verification

8.1 Description of Process/Measurement Setup

All spiral inductors were fabricated in Philips Semiconductors Qubic2 BiCMOS process. Approximate process parameters are given in Table I. Inductors are fabricated on metal 2 to minimize the series loss and to maximize the distance of the inductors from the substrate. Metal 1 is used as the "bridge layer" to make connections to the inner turn of the spiral.

Metal 2	$R_{sh} = 33m\Omega/sq$	thickness = 1.27μm	C_{sub}=14aF/μm^2
Metal 1	$R_{sh} = 50m\Omega/sq$	thickness = 1.00μm	C_{sub}=21aF/μm^2
Metal 0	$R_{sh} = 100m\Omega/sq$	thickness = 0.40μm	C_{sub}=105aF/μm^2
Buried Layer	$\rho = 0.085\Omega$-cm	thickness = 1μm	p$^+$ Si
Bulk Substrate	$\rho = 20\Omega$-cm	thickness = 675μm	p$^-$ Si

Table I. Approximate Process Parameters
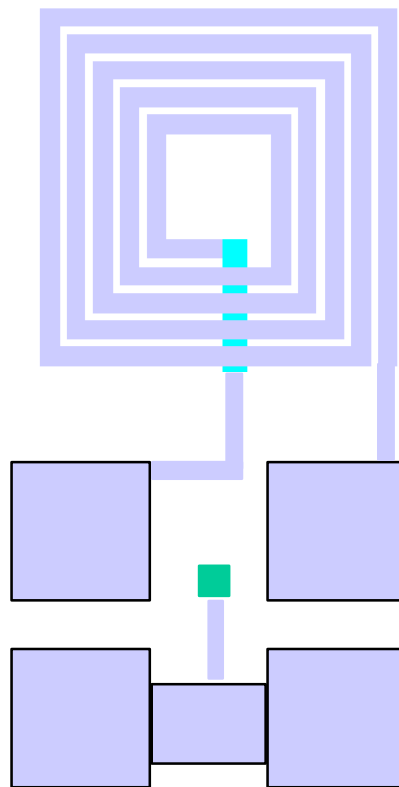
Fig. 1a. Layout of spiral and probe pads for measurement.

Using on-chip cascade probes, the average two-port *s*-parameters of the spirals are measured from 100MHz - 5GHz. Since the measurement setup holds wafers in place using vacuum suction, the back-plane of the substrate is effectively floating. The substrate surface is grounded by placing substrate taps near the spirals in the layout.
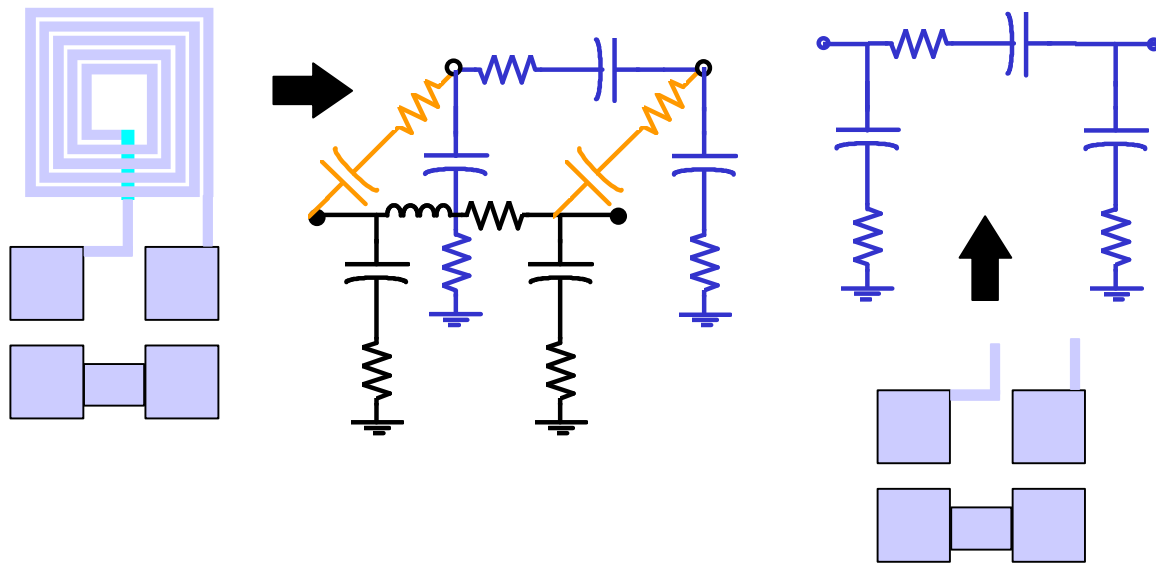
Fig. 1b. Layout and equivalent circuit models of spiral and pads used for calibration procedure.

Pad capacitance is de-embedded by subtracting out the open-circuit structure *y*-parameters from the spiral *y*-parameters. The calibration procedure we use is the standard approach and is reported widely. But there is an intrinsic problem with this calibration approach which can render the measurement results inaccurate. Fig. 1a shows the layout of a typical spiral setup for measurement. To de-embed the large substrate capacitance and resistance of the pad structure, the open-pad two-port parameters are also measured, as shown in Fig. 1b. In the same figures we show a schematic of the pad parasitics along with the spiral equivalent circuit. Clearly, the open-circuit pad structure does not contain the parasitic coupling between the spiral structure and the pads. In addition, the pad-to-pad coupling is different in the two cases shown, since the spiral itself tends to shield the

pads from one another. Hence, the pad parasitics are not correctly de-embedded from the measurement results.

To show this effect, we simulate a sample inductor with and without pads. Next, we de-embed the pad parasitics from the simulation results with pads (just as one would in measurement) and the resulting extracted series inductance, resistance, and Q factor are shown in figures 2a and 2b. The inductance value is in error but in both cases increases with frequency; the series resistance values, though, deviate dramatically as a function of frequency. Notice too that the trend comes out incorrect, increasing as a function of frequency instead of decreasing. Also shown is the resulting error in the Q factor. Notice too that this error can change the location of the peak Q-factor, resulting in sub-optimal designs. Not shown are the equivalent extracted substrate impedance values. The measurement errors can produce dramatic differences here too, changing the substrate resistance by a factor of 2. The substrate capacitance can actually change sign due to resonance phenomena. In the following sections, in order to match simulation results to measurements, we simulated our structures under the same conditions as they were measured.
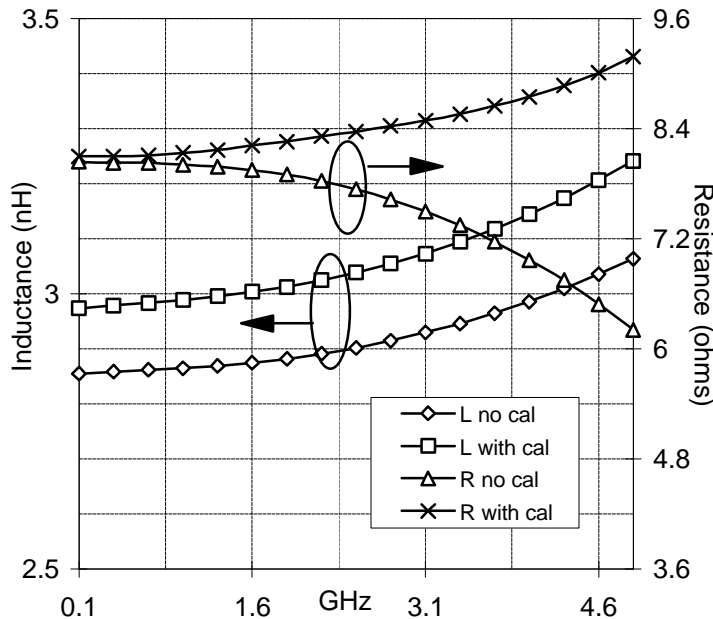
Fig. 2a. Extracted inductance and resistance of spiral inductor with and without calibration procedure.
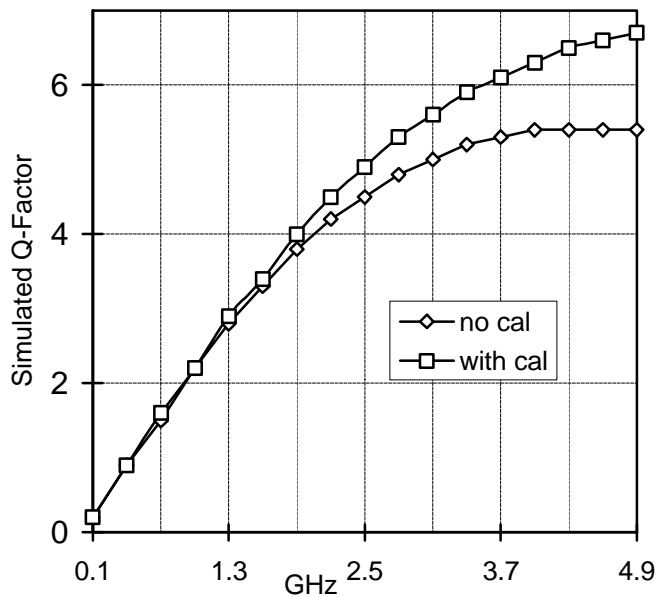
Fig. 2b. Extracted quality factor Q with and without calibration procedure.

To solve these problems, we can of course always minimize the parasitic coupling between the device under test and the pads by physically moving the structure away from the pads and by placing isolating substrate taps between the structures. Nevertheless, this requires large areas to be consumed on the chip. While this calibration problem occurs for a BiCMOS substrate, simulation also indicates some problems on an epitaxial CMOS substrate. The magnitude of the error, though, is much smaller. For instance, the series L and R change much less and only the substrate impedance changes drastically due to the calibration step.

8.2 Extraction of Circuit Parameters from Measurement Data

At each frequency of interest, the equivalent pi-circuit of Fig. 6.1a can be extracted from y-parameters. By taking real and imaginary parts of Y_{12}, equivalent inductance and resistance are extracted. Similarly, input and output shunt capacitance and resistance to substrate may be extracted by taking real and imaginary parts of $Y_{11}+Y_{12}$ and $Y_{22}+Y_{12}$. Since the circuit is passive, it is also reciprocal so that $Y_{12}=Y_{21}$. This extraction procedure

is widely used and is simple to implement since the electrical parameters of the spiral are uniquely determined at each frequency. The drawback, though, is that the extracted inductance is not physical and contains the effects of the capacitive coupling which tends to boost the inductance as a function of frequency, similar to a parallel tank. The extraction technique presented in [34] is superior in this regard.

To extract Q using Fig. 6.1a one can define the input or output Q by the two-port parameters. Looking into port 1

$$Q_1 = \frac{-\text{Im}(Y_{11})}{\text{Re}(Y_{11})} \tag{1}$$

The above definition has the awkward property that the Q is zero at self-resonance. Since inductors are usually operated far from self-resonance, this does not present too many problems. But in some applications, the inductor is used as a resonant tank close to self-resonance. In such cases, it is more appropriate to define the Q using a 3dB bandwidth definition

$$Q = \frac{w_0}{\Delta w_{3dB}} \tag{2}$$

Equally applicable, one may use the rate of change of phase at resonance

$$Q = \frac{w_0}{2} \left. \frac{df}{dw} \right|_{w_0} \tag{3}$$

The above equations are derived using second-order resonant circuits. For higher order circuits, perhaps the best definition is based on ratio of energy stored in the circuit to energy dissipated per cycle, or

$$Q = \left. \frac{W_{stored}}{W_{diss}} \right|_{per\ cycle} \tag{4}$$

For circuits, though, the best approach to defining Q should be application dependent. For instance, to minimize oscillator phase noise, one requires the rate of change of phase to be maximum at resonance, as in equation (3). Equivalently, for a narrow-band tuned load one wishes to minimize the bandwidth of the device, as in equation (2). Our approach to Q extraction is based on equation (3).
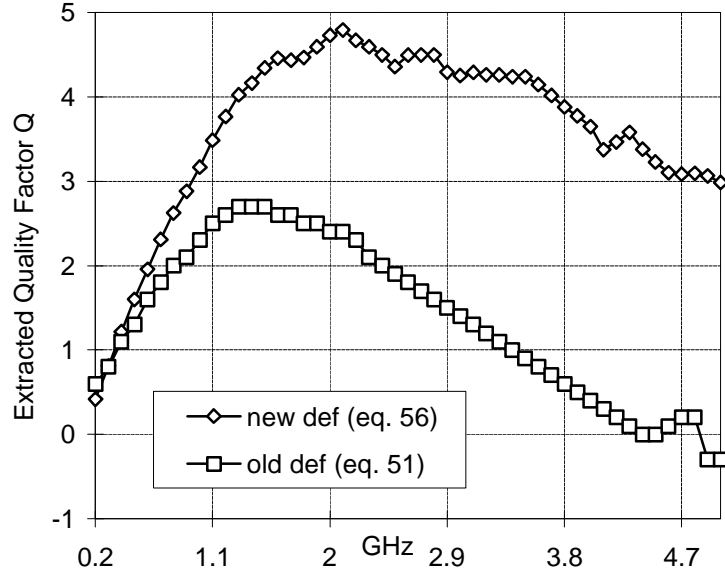
Fig. 3. Extracted quality factor Q of a 9 turn square spiral by using equations (1) and (6).

At each frequency of interest, an ideal capacitor is inserted in shunt with the inductor with admittance equal to the imaginary part of Y_{11}. The resulting admittance becomes

$$Y'(w) = jwC + Y_{11} \qquad\qquad C = -\frac{\text{Im}[Y_{11}(w_0)]}{w_0} \qquad\qquad (5)$$

This capacitance will resonate the device at the frequency of interest w_0. By examining the rate of change of phase one can find the equivalent Q

$$\left.\frac{dj}{dw}\right|_{w_0} = \frac{2Q}{w_0} = \frac{\angle Y'(w_0 + dw) - \angle Y'(w_0 - dw)}{2dw} \qquad\qquad (6)$$

To illustrate this approach, in Fig. 3 we plot the Q of a typical spiral inductor (square spiral with 9 turns of dimensions given in the next section) using the definition present in (6). In the same plot we show the traditional definition of Q, using (1). As we approach self-resonance, the two definitions deviate greatly. Notice also that the peak value of Q occurs at different frequencies for the two definitions.

In the following sections on measurement results, the data is measured at room temperature. It is important to calculate Q at the frequency and temperature of interest [33]. At low frequencies the Q temperature coefficient (TC) will depend on the metal TC whereas at high frequency the Q will change due to the TC of the substrate resistance.
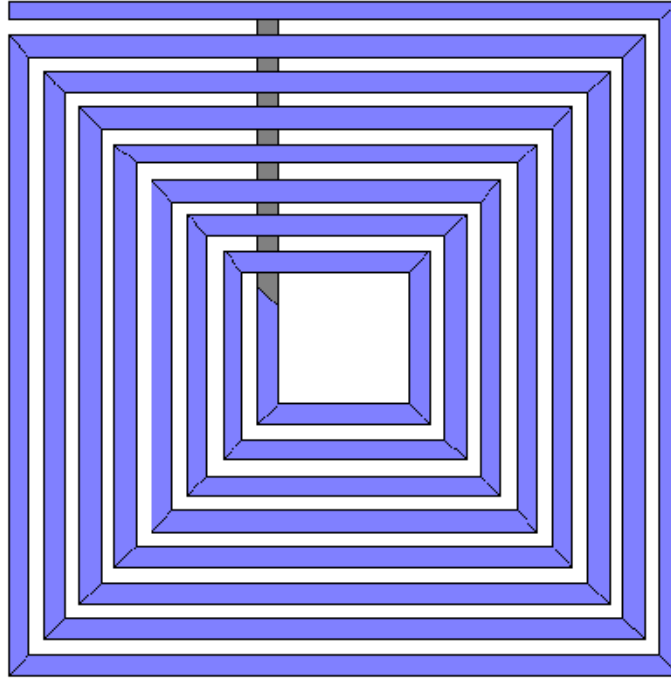
Fig. 4. Layout of 8 turn spiral.

9.3 Square Spiral Inductors

Since square spirals are the most common inductors in Si RF ICs, we begin by comparing our simulation results of the previous section with measurement results. Many square spirals were fabricated and measurement results were compared to simulation. The spirals have the following geometry: Constant inner area, A_i = 44μm, constant width w = 7μm, and constant spacing s = 5μm, with turns n = 5-10. A chip layout of the 8-turn spiral appears in Fig. 4. For example, Fig. 5 shows the measured and simulated s-parameters for the 8 turn spiral.   As can be seen from the figure, simulation s-parameters match the measured s-parameters well.   The simulation time is under a minute per frequency point.

Fig. 6a plots of the extracted series inductance from both measurement data and simulation data for the 5-turn and 8-turn spirals. Good agreement is found for all spirals.
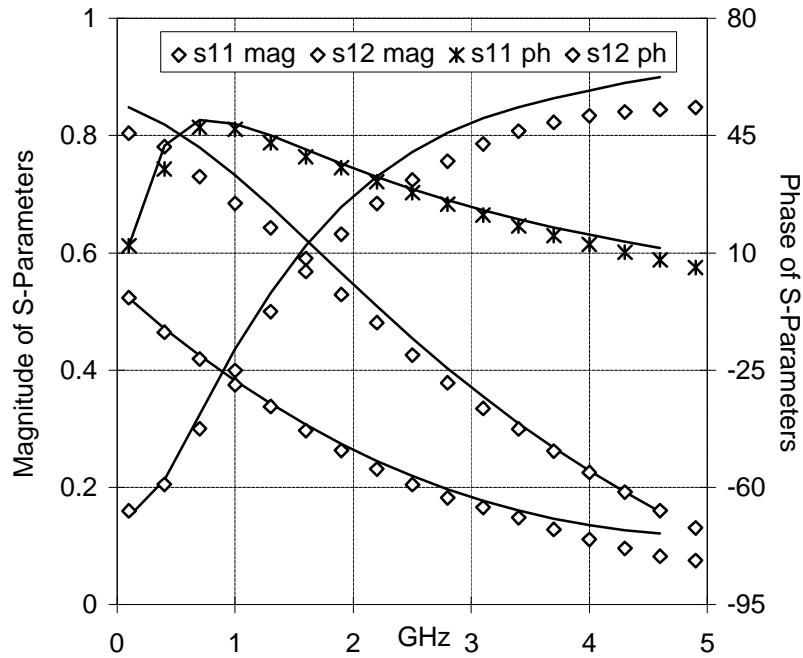
Fig. 5. Measured and simulated *s*-parameters of the 8 turn square spiral.

For all spirals, the inductance is an increasing function of frequency. This is due primarily to the coupling capacitance which boosts the effective *L* as a function of frequency. For the smaller spirals, the same coupling capacitance tends to increase *R* as well, but the effect of the shunt substrate resistance is to lower the effective series *R*. For large spirals in which substrate injection occurs at a lower frequency, the behavior of *R* is a decreasing function of frequency. For smaller spirals, the substrate injection is minimal due to a small substrate capacitance, and the effect of the coupling capacitance boosts *R* as a function of frequency.

Fig. 6b shows the Q-factor for the 5-turn and 8-turn spirals. Here, we used the phase definition of equation (6) to compute Q. Good agreement is found between measurements and simulations. For the smaller 5-turn spiral the Q is an almost linear function of frequency, demonstrating that the substrate has negligible effects on the spiral and the Q is approximately given by wLR^{-1}. The larger 8-turn spiral, though, shows more complicated behavior due to the substrate. At low frequencies when the substrate

65
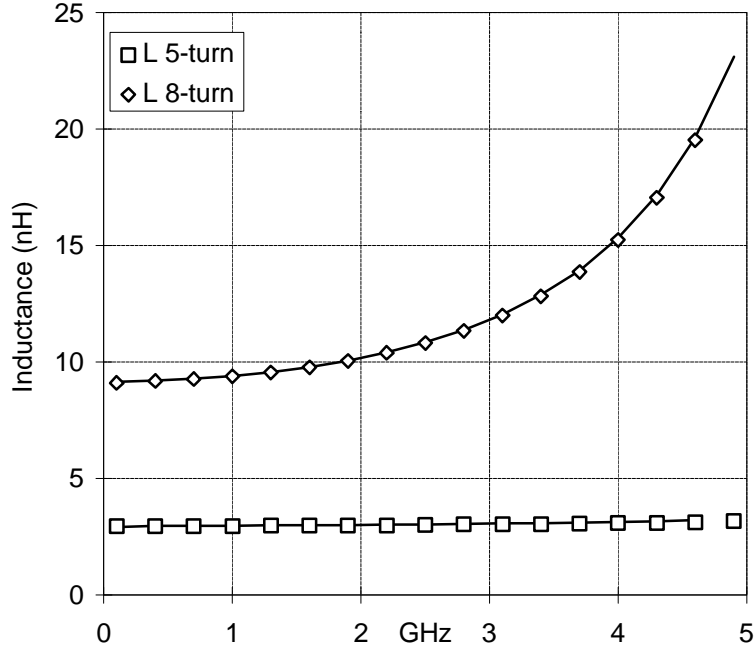
Fig. 6a. Extracted inductance of square spirals from measurements and simulation.

impedance is large, the simple linear behavior is observed. At high frequencies, when the substrate impedance is smaller than the inductive/resistive impedance of the spiral, the substrate loss dominates and the Q is a decreasing function of frequency. In the frequency range of interest, the Q is a combination of the above mentioned effects, and the Q peaks at some frequency, f_{QMAX}. Notice that our analysis predicts this frequency well. This is important since we can design inductors that have peak Q at the frequency of interest.

Using the modeling described in section IV.A, we model the inductors using the equivalent circuits of Fig. 6.1b. Table II compares our results, including the total error involved in the modeling. The error is derived by computing the relative error between the two-port measured *s*-parameters and the model two-port *s*-parameters. The error is cumulative over 16 points in the frequency range. Two models were generated, one model is based on the actual measurement results whereas the other model is based solely on simulation results (the simulation model is not a curve-fitted model of the measurements, but rather a curve-fit to the simulations).
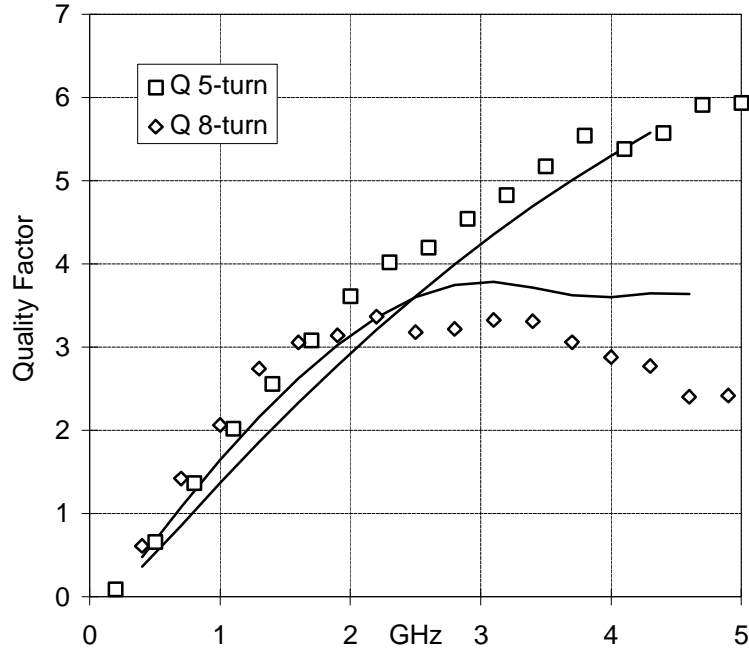
Fig. 6b. Extracted Q-factor of square spirals from measurements and simulation.

Model Parameter	Measured 5-turn	Simulated 5-turn	Measured 8-turn	Simulated 8-turn
L (nH)	2.93	2.97	8.78	8.55
R (Ω)	8.02	8.23	17.50	16.99
C_{s1} (fF)	93.5	174.4	176.9	152.6
C_{s1} (fF)	210.7	341.8	656.6	179.9
R_{s1} (Ω)	1.35k	377	527.6	290.2
R_{s2} (Ω)	1.06k	472	587.0	314.7
C_{BR} (fF)	22.4	88.9	63.4	106.2
Σ error^2	.06	0.30	0.37	0.52

Table II. Simulated and Measured Models For Square Spirals

9.4. Polygon Spiral Inductors

Since polygon spirals with more than four sides have higher Q than square spirals (for the same area), it is advantageous to use these structures. Many spirals are measured and compared with simulation. The geometry of the fabricated spirals is shown in Table III. A chip micro-photograph of a sample spiral inductor L4 appears in Fig. 7. *S-*

Spirals	L4	L6	L7	L8	L9	L11
Radius R (μm)	105	105	105	105	105	105
Width W (μm)	8.2	7.5	7.5	7.5	7.5	6.5
Space S (μm)	3	3	3	3	3	3
Turns N	6.75	8	8	8	8	7.75
No. of sides	12	12	12	12	12	12
Metal (s)	M2	M2	M1+M2 via[(+)]	M1+M2 via[(-)]	M1+M2 +M3	M2

Table III. Polygon Spiral Geometry

parameters are plotted for the L4 spiral in Fig. 8 and again good agreement is found between simulation and measurement. Extracted series inductance and Q for the L4 and L11 spirals are plotted in figures 9ab. The inductors are also modeled using the equivalent circuit of Fig. 6.1b, and Table IV summarizes the model parameters based on
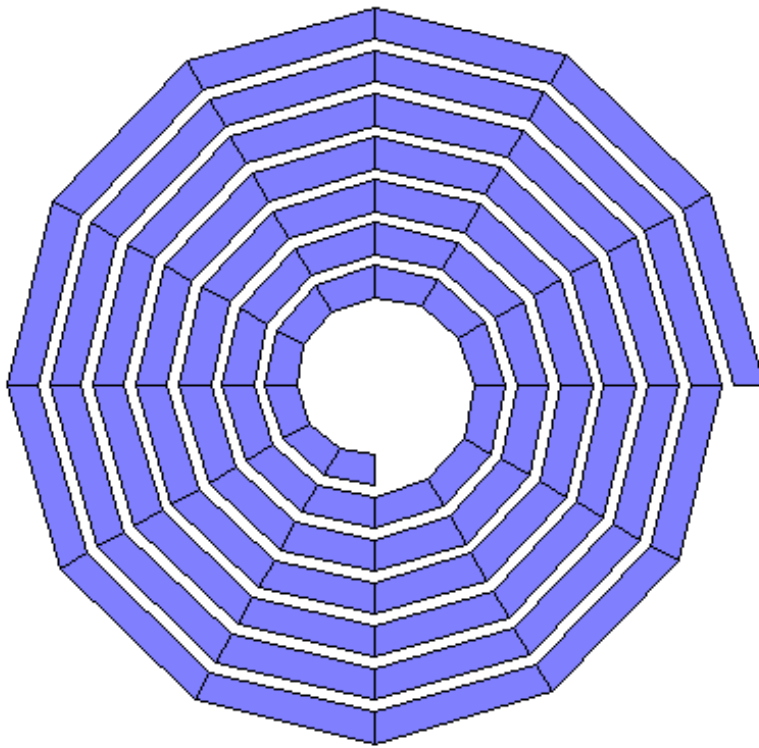
Fig. 7. Layout of polygon spiral inductor L4.

measurement and simulation.

| Model Parameter	Measured L4	Simulated L4	Measured L11	Simulated L11
L (nH)	5.45	5.67	7.3	7.7
R (Ω)	10.3	11.5	16.0	16.4
C_{s1} (fF)	132	225	134	208
C_{s1} (fF)	336	280	320	258
R_{s1} (Ω)	765	711	762	832
R_{s2} (Ω)	726	723	769	869
C_{BR} (fF)	45	55	45	55
Σ error^2	0.02	0.20	0.07	0.24

Table IV. Simulated and Measured Models For Polygon Spirals
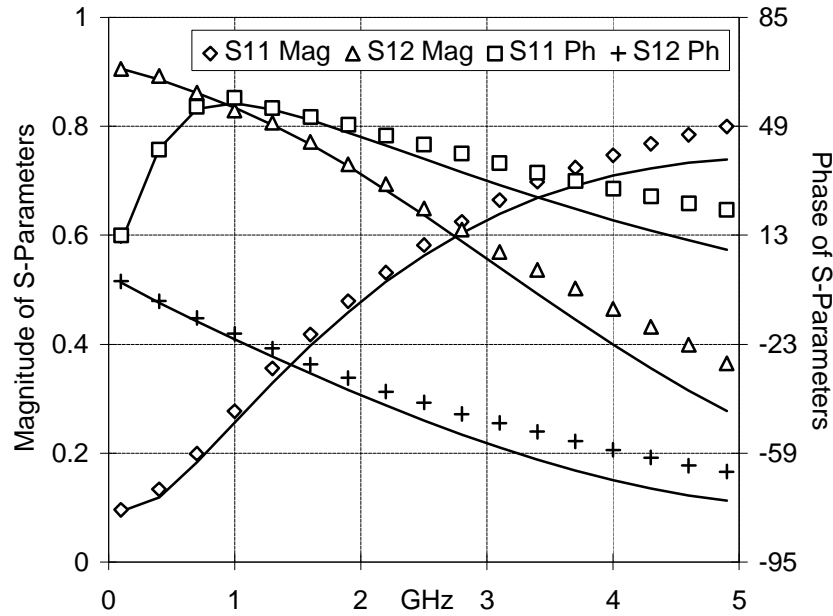
Fig. 8. Measured and simulated *s*-parameters of the L4 polygon spiral.
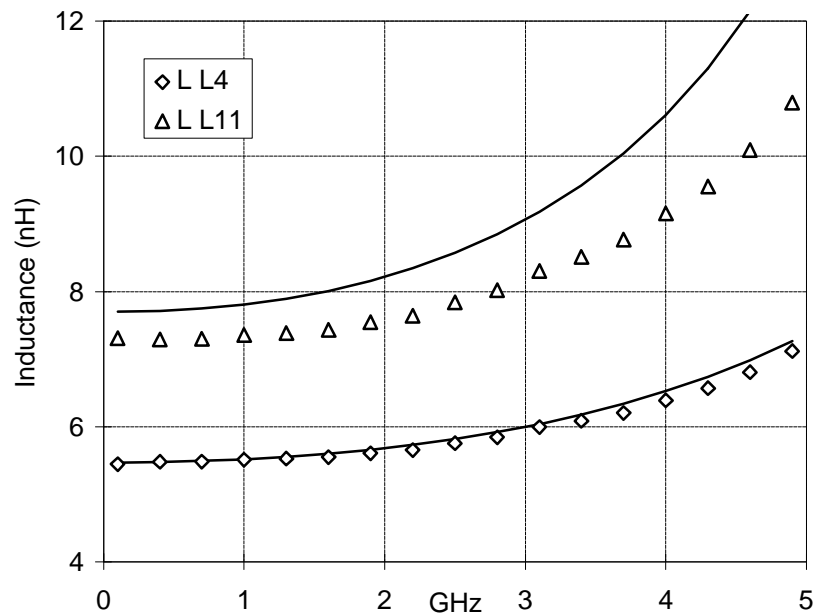
Fig. 9a. Extracted inductance of polygon spirals from measurement and simulation.
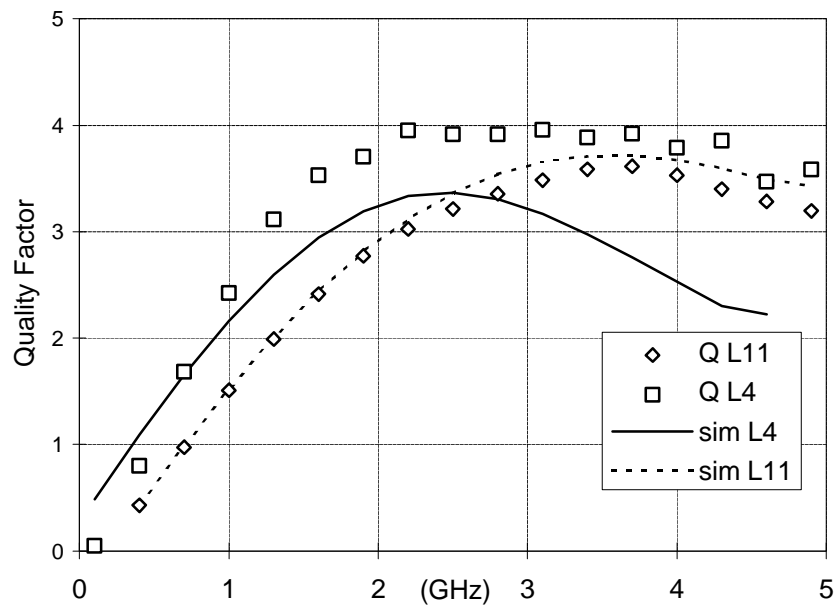
Fig. 9b. Extracted Q-factor polygon spirals from measurement and simulation.

8.5 Multi-Metal Spiral Inductors

To improve the low-frequency Q of the spiral, we can place metal layers in shunt as discussed in section IV.B. To test this, the spiral L6 in the polygon set was used. Three new inductors L7, L8, and L9 were constructed. L7 has two L6 spirals on metal 2 and metal 1 connected in shunt with as many vias as possible; L8 also has two L6 spirals in shunt, but with vias placed only at the ends of the segments. Finally, L9 has all metals connected in shunt (except where it was necessary to use metal 0 to connect to the inner turn of the spiral).
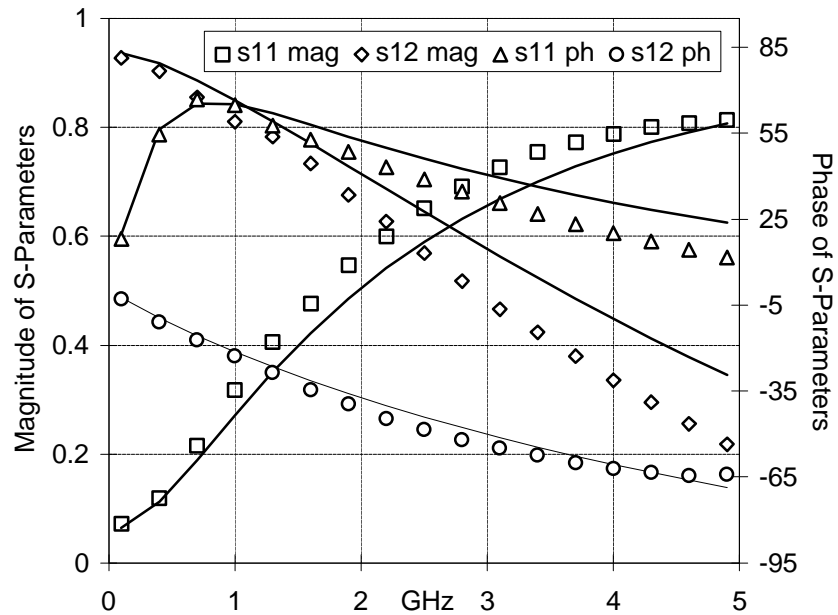
Fig. 10. Measured and simulated *s*-parameters of the M1-M2 multi-metal polygon spiral L7.
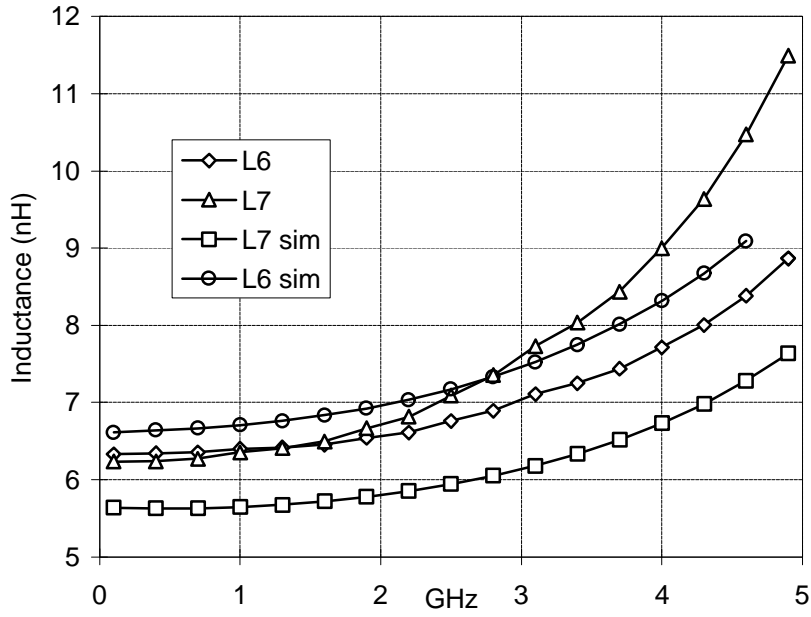
Fig. 11a. Extracted inductance of polygon spirals L6 and L7.
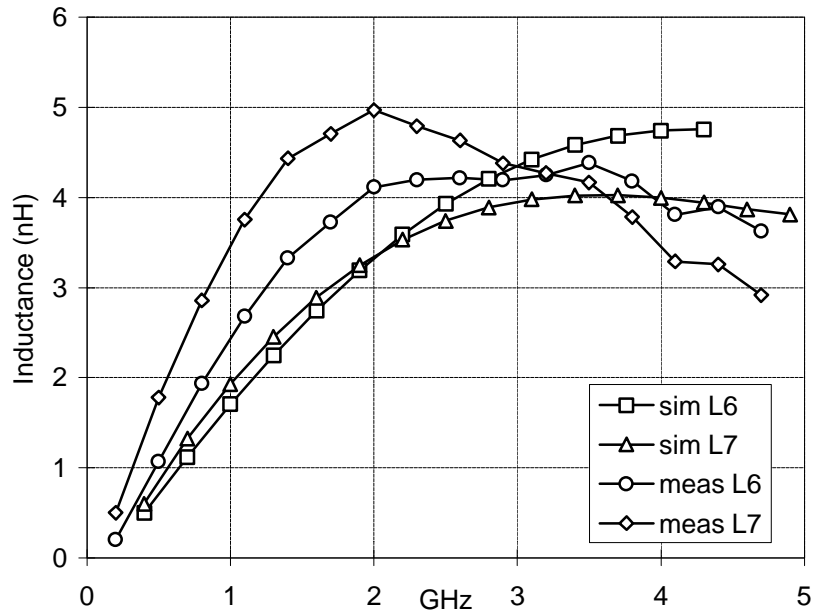
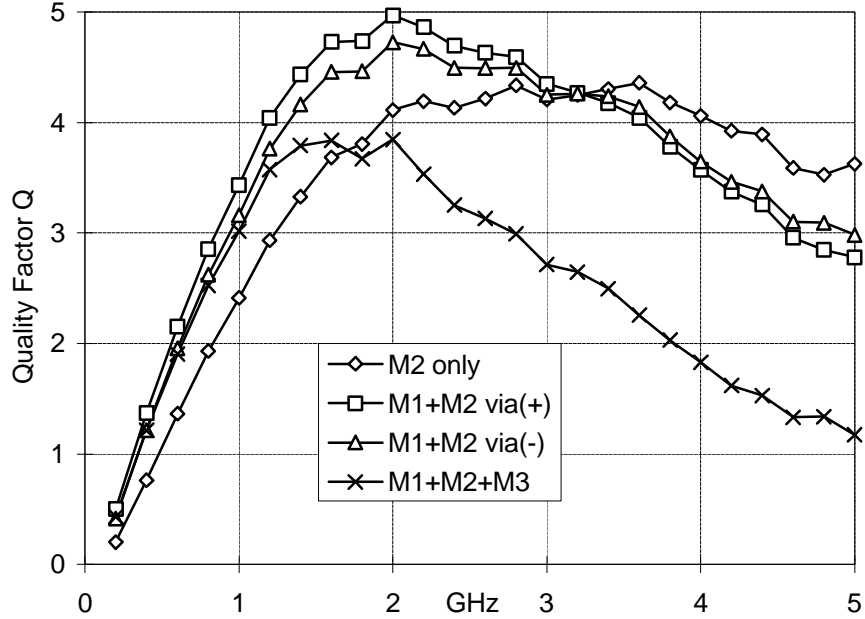Fig. 11b. Extracted quality factor of polygon spirals L6 and L7.

Fig. 12. Measured Q-factor enhancement of multi-metal shunt connected spirals.

Simulations were run for the M2+M1 spiral and measured and simulated *s*-parameters are shown in Fig. 10. Good agreement is found as before. Fig. 11a plots the extracted series inductance of the spirals. Due to the tight coupling the inductance value of the metal-metal structure does not drop much. Fig. 11 plots the extracted Q of the spirals. The low-frequency Q enhancement of the metal-metal structure is due to the drop in series resistance. The series resistance drop is in accordance with connecting the appropriate metal layers in shunt. At high frequency, though, the picture changes greatly due to substrate loss. At high frequency the Q of the single metal layer is actually better.

Figure 12 compares the measured Q of L6, L7, L8, and L9. The measurement results indicate an overall Q-increase at low frequency for the M1+M2 cases, but using three metal layers is actually harmful at all frequencies (since the M0 layer is very close to the substrate). Also, the Q of L8 is slightly higher than the Q of L7 demonstrating that use of ample vias helps to boost the Q in the shunt configuration.

8.6 Coupled Spiral Inductors

Many RF IC designs incorporate several spiral inductors on the same die. Since these structures are physically large, substrate coupling can be a significant problem. For instance, in any amplification stage the substrate coupling can act as parasitic feedback, lowering the gain and possibly causing oscillations to occur. Hence, it is very important to model the substrate coupling.

The analysis technique presented in 3.2 is directly applicable here. The *s*-parameters of two 8 turn square spirals separated by a distance of 100μm were simulated and measured. Fig. 13 shows the magnitude of the measured and simulated s-parameters. As can be seen from the figure, simulation results predict the coupling behavior accurately, such as the minimum S_{21}. To gain further insights into the coupling, we plot the power isolation from one spiral to the other using the following equations. For the arbitrary passive two-port shown in Fig. 14a., the ratio of the power delivered to a resistive load R_L through the two-port can be shown to be
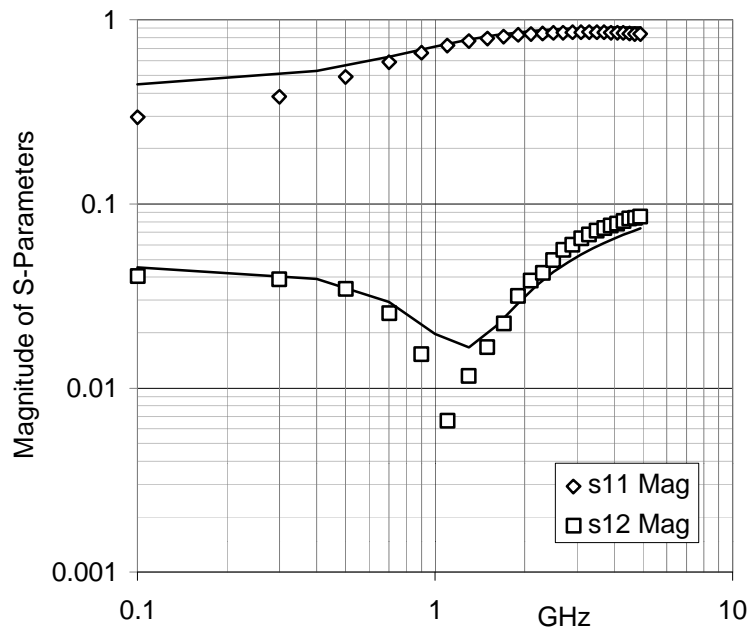
Fig. 13. Measured and simulated *s*-parameters of the coupled spirals.

$$\frac{P_L}{P_{in}} = \frac{R_L \|G_I\|^2}{\text{Re}[Z_{in}]} \tag{7}$$

In the above equation, G_I is the current gain through the two port and Z_{in} is the impedance looking into the two-port from the source side

$$G_I = \frac{z_{12}}{R_L + z_{12}} \tag{8}$$

$$Z_{in} = z_{11} - \frac{z_{12}^2}{R_L + z_{22}} \tag{9}$$

Using the above equations we plot the measured and simulated power isolation for the coupled inductors in Fig. 14b, where a 50 Ω load resistance is used in the above equations. Clearly, there are two frequencies where the isolation is maximum. These frequencies depend on the geometrical layout of the spirals and hence this gives the designer the powerful option of placing the spirals in locations to maximize isolation.
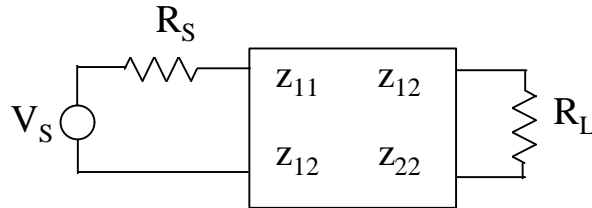

Fig. 14a. Circuit for calculating the power delivered to a resistive load from a reciprocal two-port.
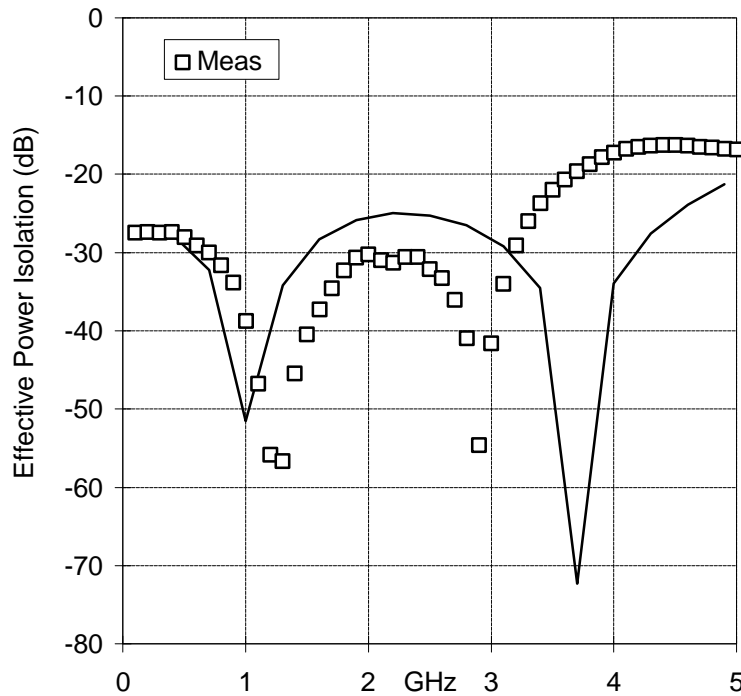

Fig. 14b. Measured and simulated power isolation between the coupled spirals.

8.7 Planar Transformers

To test the simulation accuracy for transformers, several planar transformers were fabricated and measured. An example transformer structure is shown in Fig. 15. The

Transformer Model Parameter	Measured	Simulated
L (nH)	4.88	4.63
R (Ω)	17.58	16.91
C_s (fF)	124	123
C_p (fF)	430	418
R_s (Ω)	243	252
R_C (Ω)	1.00k	796
$C_{1,2}$ (fF)	53	59
$k_{1,2}$	.703	0.715
$\Sigma \, \text{error}^2$	0.79	0.04

TableV. Simulated and Measured Models For Planar
Transformer

transformer is made of two interwound spirals each of 5-turns of 7µm wide metal with a spacing of 17 µm. Measured and simulated s-parameters are shown in Fig. 16. Again, good agreement is found between simulation and measurement. We can gain further
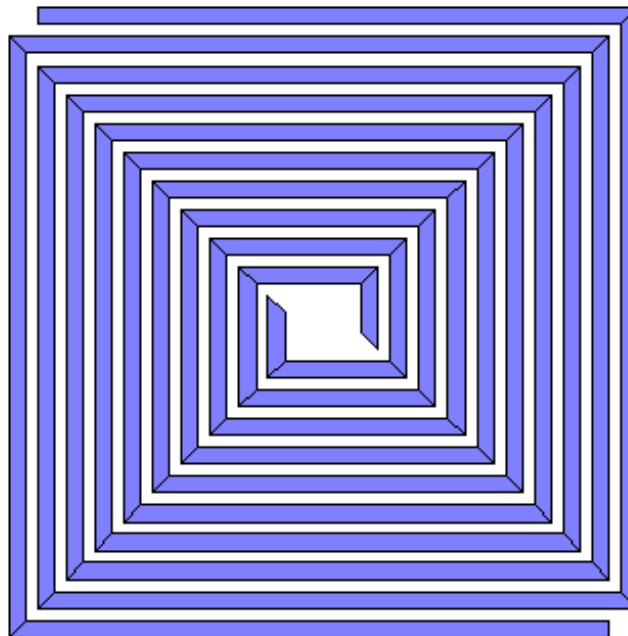

Fig. 15. Layout of planar transformer.

insight into the measurement results by using equation (7). We plot the measured and simulated loss in Fig. 17. Again we use a 50 Ω load resistance value. But since the loss is a function of load resistance, one would typically find the optimal value at the frequency of interest to minimize losses.

The dynamics of the transformer can be captured in a compact model similar to the coupled inductors, as shown in Fig. 6.7.a. The *k* factor for planar inductors is about 0.7 to 0.8. Substrate coupling is again modeled with R_C. While the circuit of Fig. 6.7.a is physically based, one can also derive the equivalent circuit shown in Fig. 6.7.b, which contains an ideal transformer at the core with parasitic elements. The model parameters from measurement and simulation appear in Table V.
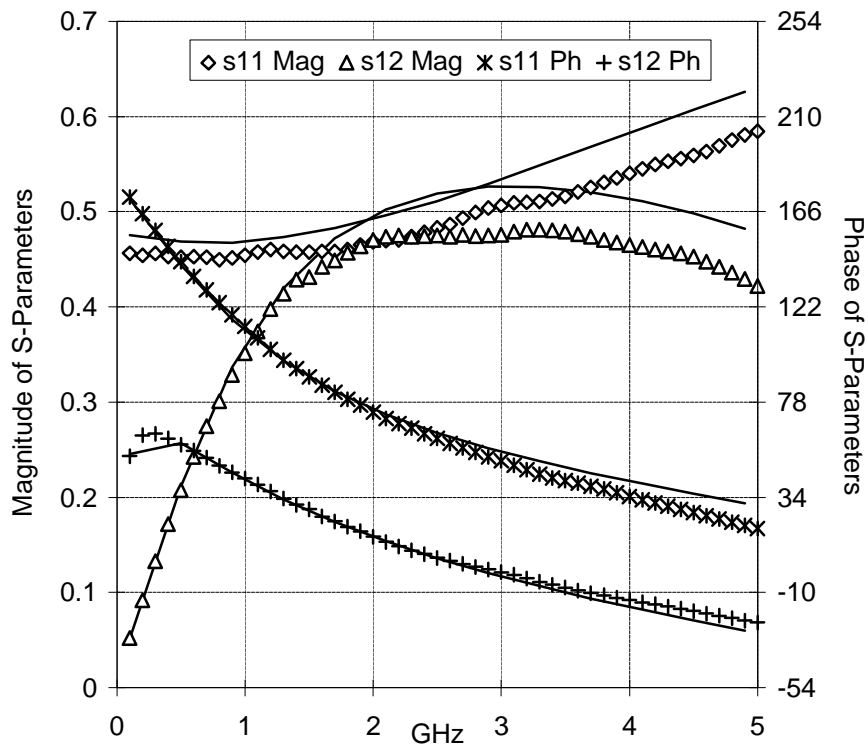

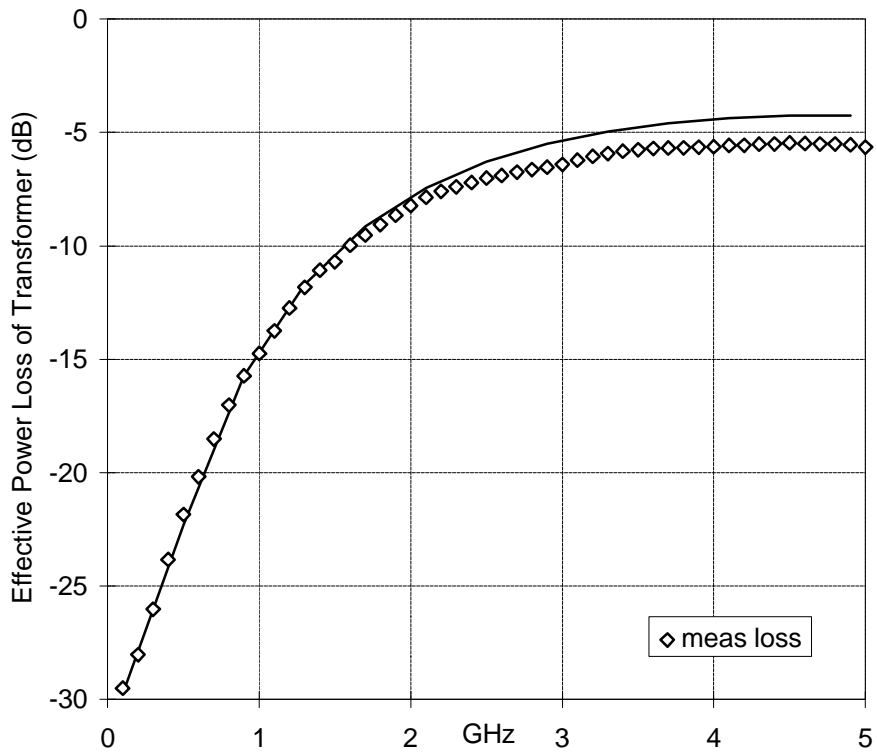Fig. 16. Measured and simulated *s*-parameters of planar transformer.

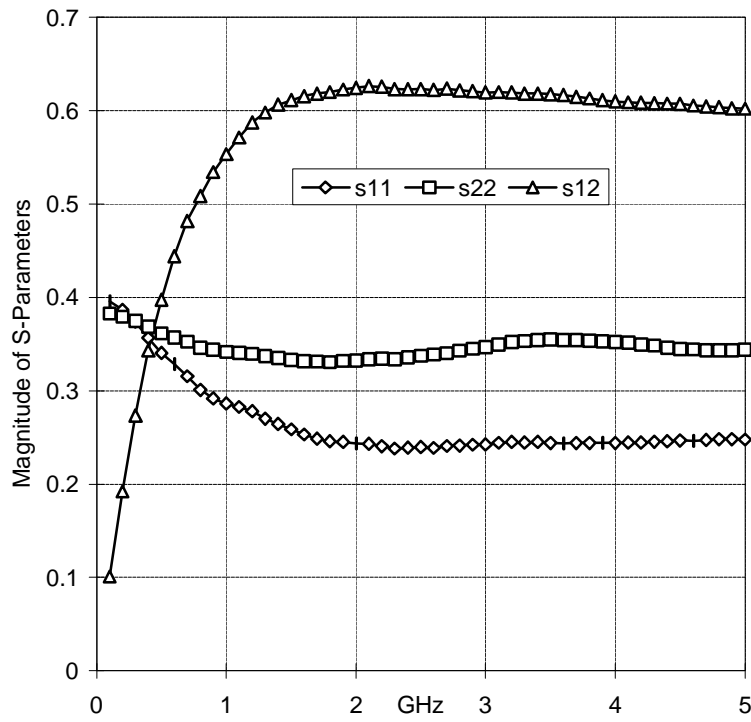Fig. 17. Measured and simulated power loss of planar transformer.

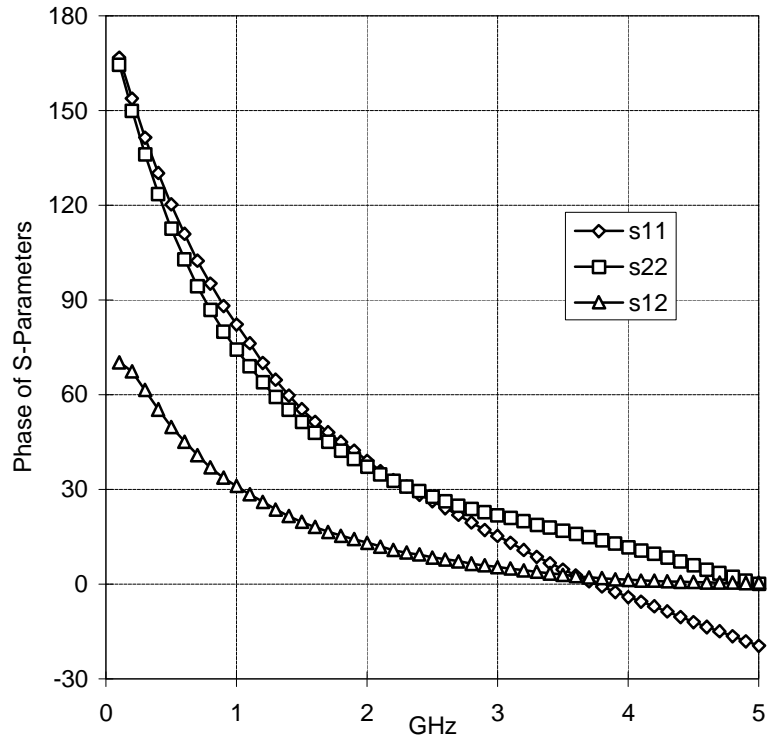Fig. 18a. Magnitude of measured *s*-parameters for metal-metal transformer.

Fig. 18b. Phase of measured *s*-parameters for metal-metal transformer.

8.8 Metal-to-Metal Transformers

Planar transformers consume large areas on the Si die. To save area, one may use multiple metal layers to design transformers. The straightforward approach is to use two spirals on top of each other. The measured *s*-parameters of such a structure is shown in Fig. 18ab. As evident from the figure, even though the spirals are identical, the structure is non-symmetric due to the extra series loss of metal 1 and the extra capacitance and substrate loss associated with metal 1. In order to design a more symmetric structure, one may split up the primary and secondary and layout half of the primary on metal 1 and half on metal 2. Such a structure is shown in Fig. 19. Measured s-parameters for such a structure are shown in Fig. 20. Clearly, this structure is more symmetric.
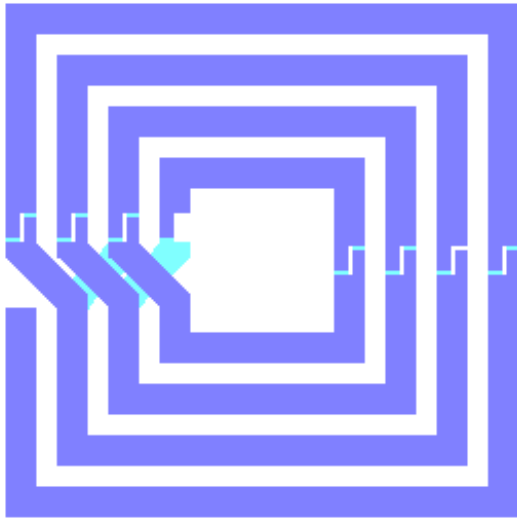
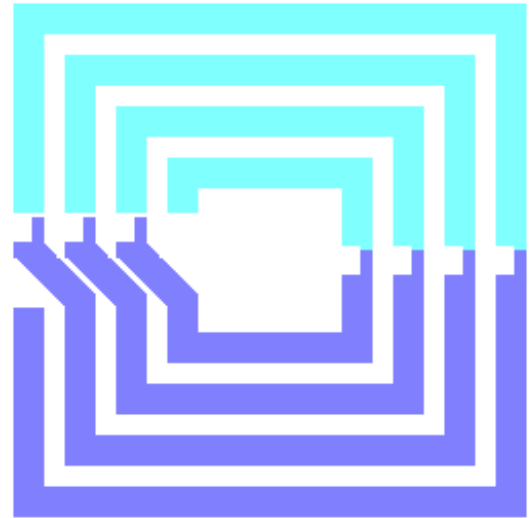Fig. 19a. Layout of symmetric metal-metal transformer.　　　Fig. 19b. One winding of symmetric metal-metal transformer.

In general, metal-metal transformers suffer from high parasitic coupling from the primary to the secondary, making these devices unsuitable in most applications. On the
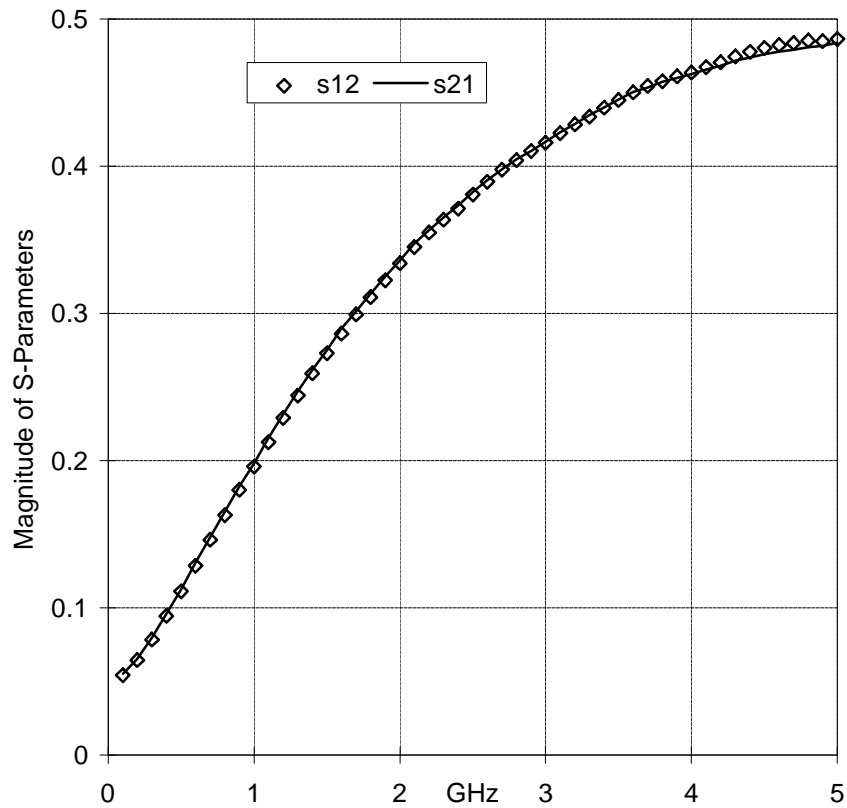

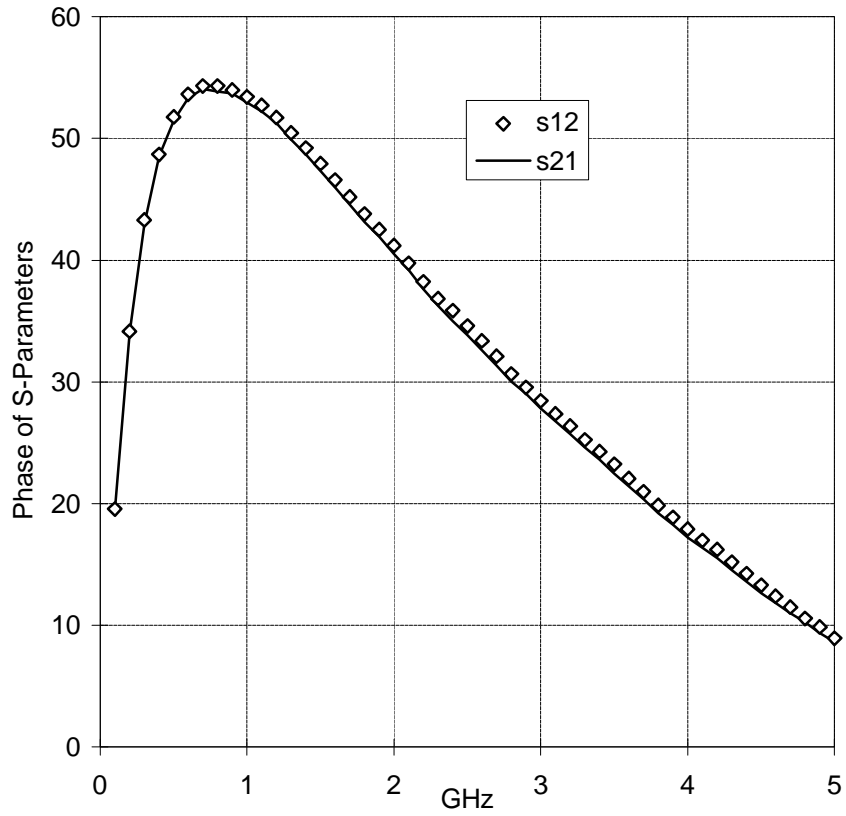Fig. 20a. Measured magnitude *s*-parameters of metal-metal symmetric transformer.

Fig. 20b. Measured phase *s*-parameters of metal-metal symmetric transformer.

other hand, the *k* factor is slightly larger than the planar transformer and a lot less area is consumed.

Chapter 8: Conclusion

In this thesis we have presented techniques to analyze, model, and optimize spiral inductors and transformers on the Si substrate. The techniques are accurate, taking into account substrate coupling, current constriction, and proximity effects. The analysis is also fast and efficient, making it suitable for computer optimization. Furthermore, the analysis is general and appropriate for analyzing any arbitrary arrangement of conductors, such as multi-metal spirals. A custom CAD tool *ASITIC* was developed which incorporates the algorithms discussed in this paper. *ASITIC* was used to analyze a wide variety of test structures such as square spirals, polygon spirals, coupled spirals, and transformers. The test spirals were also fabricated and measurement results compared well to simulation on a BiCMOS substrate. Compact models for the various devices were presented which model the device dynamics over a wide frequency range.

There are many areas, though, where the work can be improved. For instance, while the capacitance matrix calculation was fairly general, taking the effect of the substrate into account, our inductance matrix calculation assumed the effects of the substrate to be negligible.   While this was substantiated with measurement results on a BiCMOS substrate, more study needs to be performed on the CMOS substrate since the highly conductive bulk substrate of the CMOS epi process is likely to cause extra components of loss at high frequency due to eddy-currents.   Thus, the inductance matrix calculation should be performed in an analogous fashion to the capacitance matrix calculation, with an appropriate Green function representing the substrate loss.

References

[1]   N. M. Nguyen and R. G. Meyer, "Si IC-compatible inductors and *LC* passive filters," *IEEE J. Solid-State Circuits*, vol. 27, no. 10, pp. 1028-1031, Aug. 1990.

[2]   K. B. Ashby, W. C. Finley, J. J. Bastek, S. Moinian, and I. A. Koullias, "High Q inductors for wireless applications in a complementary silicon bipolar process," in *Proc. Bipolar and BiCMOS Circuits and Technol. Meet.*, Minneapolis, MN, 1994, pp. 179-182.

[3]   J. N. Burghartz, M. Soyuer, and K. Jenkins, "Microwave inductors and capacitors in standard multilevel interconnect silicon technology," *IEEE Trans. Microwave Theory Tech,* vol. 44, no. 1, pp. 100-103, Jan. 1996.

[4]   R. B. Merrill, T. W. Lee, Hong You, R. Rasmussen, and L. A. Moberly, "Optimization of high Q integrated inductors for multi-level metal CMOS," *IEDM* 1995, pp. 38.7.1 - 38.7.3.

[5]   L. Zu, Y. Lu, R. C. Frye, M. Y. Law, S. Chen, D. Kossiva, J. Lin, and K. L. Tai, "High Q-factor inductors integrated on MCM Si substrates," *IEEE Transactions on Components, Packaging and Manufacturing Technology*, Part B: Advanced Packaging, Aug. 1996, vol.19, no.3, pp. 635-43.

[6]   J. Y.-C. Chang and A. A. Abidi,"Large suspended inductors on silicon and their use in a 2-μm CMOS RF amplifier," *IEEE Electron Device Letters*, vol. 14, no. 5, pp. 246-248, 1993.

[7]   J. R. Long and M. A. Copeland, "The modeling, characterization, and design of monolithic inductors for silicon RF IC's," *IEEE J. of Solid-State Circuits*, vol. 32, no. 3, pp. 357-369, Mar. 1997.

[8]   J. Craninckx and M. Steyaert, "A 1.8-GHz low-phase-noise CMOS VCO using optimized hollow spiral inductors," *IEEE J. Solid-State Circuits*, vol. 32, no. 5, pp. 736-745, May 1997.

[9]   D. Lovelace, N. Camilleri, "Silicon MMIC inductor modeling for high volume, low cost applications," *Microwave Journal,* pp. 60-71, Aug. 1994.

[10]   S. Ramo, J. R. Whinnery, and T. Van Duzer, *Fields and Waves In Communication Electronics*. 3rd ed., John-Wiley and Sons, Inc, 1994, pp. 324-330.

[11]   W. T. Weeks, L. L. Wu, M. F. McAllister, and A. Singh, "Resistive and inductive skin effect in rectangular conductors," *IBM J. Res. Develop.*, vol. 23, pp. 652-660, Nov. 1979.

[12]   M. Kamon, M. J. Tsulk, and J. K. White, "FASTHENRY: a multipole accelerated 3-D inductance extraction program," *IEEE Trans Micrwoave Theory Tech*, vol. 42, no. 9, pp. 1750-57, Sept. 1994.

[13]   D. M. Pozar, *Microwave Engineering*. 1990 Addison-Wesley, p. 233.

[14]   A. E. Ruehli, "Inductance calculations in a complex integrated circuit environment," *IBM J. Res. Develop.*, vol. 16, pp. 470-481, Sep. 1972.

[15]   F. W. Grover, *Inductance Calculations.* Princeton, N.J.: Van Nostrand, 1946, reprinted by Dover Publications, New York, 1954.

[16]   E. Pettenpaul, H. Kapusta, A. Weisgerber, H. Mampe, J. Luginsland, and I. Wolff, "CAD models of lumped elements on GaAs up to 18 GHz," *IEEE Trans. Microwave Theory Tech.*, vol. 36, no. 2, pp. 294-304, Feb. 1988.

[17]   R. Gharpurey, private communication.

[18]   J. I. Smith, "The even- and odd-mode capacitance parameters for coupled lines in suspended substrate," *IEEE Trans. Microwave Theory Tech,* vol. MTT-19, no. 5, pp. 424-431, May 1971.

[19]   R. Garg and I. J. Bahl, "Characteristics of coupled microstriplines." *IEEE Trans. Microwave Theory Tech.*, vol. MTT-27, pp. 700-705, 1979.

[20]   J.-H. Chern, J. Huang, L. Arledge, P.-C. Li and P. Yang, "Multilevel metal capacitance models for CAD design synthesis systems," *IEEE Electron Device Letters*, vol. 13, no. 1, pp. 32-34, Jan. 1992.

[21]   G. E. Howard, J. J. Yang, and Y. L. Chow, "A multipipe model of general strip transmission lines for rapid convergence of integral equation singularities," *IEEE Trans Microwave Theory Tech*, vol. 40, no. 4, pp. 628-636, April 1992.

[22]   R. Gharpurey**, "**Modeling and analysis of substrate coupling in integrated circuits," Doctoral Thesis, University of California, Berkeley.

[24]   T. Stetzler, I. Post, J. Havens, and M. Koyama, "A 2.7V to 4.5V single-chip GSM transceiver RF integrated circuit," in *IEEE International Solid-State Circuits Conference*, 1995, pp. 150-151.

[25]   J. R. Long and M. A. Copeland, "A 1.9 GHz low-voltage silicon bipolar receiver front-end for wireless personal communications systems," *IEEE J. Solid-State Circuits*, vol. 30, no. 12, Dec. 1995.

[26]   D. O. Pederson, K. Mayaram, *Analog Integrated Circuits for Communications*. Kluwer Academic Publishers, Second Printing 1991, pp. 183-4.

[27]   B.-K Kim, B.-K. Ko, K. Lee, J.-W. Jeong, K-S. Lee, and S.-C. Kim, "Monolithic planar RF inductor and waveguide structures on silicon with performance comparable to those in GaAs MMIC," in *IEDM* 1995, pp. 29.4.1 - 29.4.4.

[28]   D. Krafesik and D. Dawson, "A closed-form expression for representing the distributed nature of the spiral inductor," *Proc. IEEE-MTT Monolithic Circuits Symp. Dig.*, pp. 87-91, 1986.

[29]   J. N. Burghartz, M. Soyuer, K. A. Jenkins, and M. Kies, "RF components implemented in an analog SiGe bipolar technology", *IEEE Proc. BCTM 1996*.

[30]   W. B. Kuhn, A. Elshabini-Riad, F. W. Stephenson, "Centre-tapped spiral inductors for monolithic bandpass filters," *Electronics Letters*, 13 April 1995, vol.31, (no.8), pp. 625-6.

[31]   J. Crols, P. Kinget, J. Craninckx, M. Steyaert, "An analytical model of planar inductors on lowly doped silicon substrates for high frequency analog design up to 3GHz," 1996 Symposium on VLSI Circuits, pp. 28-29, Honolulu, June 1996.

[32]   *ASITIC: Analysis of Si Inductors and Transformers for ICs,* http://www.eecs.berkeley.edu/~niknejad.

[33]   R. Groves, K. Stein, D. Harame, D. Jadus, "Temperature dependence of Q in spiral inductors fabricated in a silicon-germanium/BiCMOS technology," *Proc of the 1996 Bipolar/BiCMOS Circuits and Technology Meeting*, New York, NY, USA, 1996, pp. 153-6.

[34]   C. P. Yue, C. Ryu, J. Lau, T. H. Lee, S. S. Wong, "A physical model for planar spiral inductors on silicon," *International Electron Devices Meeting Technical Digest*, pp. 155-158, Dec. 1996.

[35]   C.P. Yue and S.S. Wong, "On-chip spiral inductors with patterned ground shields for si-based rf ic's", *Symposium on VLSI Circuits Digest*, pp. 85-86, June 1997.